Beatriz Prego Lopes Crispim

Licenciada em Ciências de Engenharia Mecânica

Gas Tungsten Arc Welding of Cu-Al-Mn Shape Memory Alloys

Dissertação para obtenção do Grau de Mestre em Engenharia Mecânica

Orientador: Professor Doutor João Pedro de Sousa Oliveira, Professor Auxiliar, Faculdade de Ciências e Tecnologia da Universidade Nova de Lisboa

Co-orientador: Professora Doutora Rosa Maria Mendes Miranda, Professora Associada com Agregação, Faculdade de Ciências e Tecnologia da Universidade Nova de Lisboa

Júri:

Presidente: Prof. Doutor Telmo Jorge Gomes dos Santos
Arguente: Prof. Doutor Francisco Manuel Braz Fernandes
Vogal: Prof. Doutor João Pedro de Sousa Oliveira

FACULDADE DE CIÊNCIAS E TECNOLOGIA
UNIVERSIDADE NOVA DE LISBOA

Setembro 2018

To my grandparents

Acknowledgments

Resumo

Recentemente, aplicações onde se utilizam ligas com memória de forma têm atraído interesse, devido às propriedades únicas desta classe de materiais. A sua aplicação estende-se a uma ampla variedade de sectores, tal como a indústria automóvel, aerospacial, biomédica e de construção civil.

Entre as classes existentes de materiais com memória de forma, o NiTi é o mais estudado. No entanto, as ligas à base de cobre estão a emergir como potenciais substitutos para o NiTi, devido aos seus custos mais baixos e potencial para aplicação em dispositivos de amortecimento.

A necessidade de desenvolver técnicas avançadas de união de materiais é de grande interesse, uma vez que irá permitir o aumento de potenciais aplicações de qualquer liga de engenharia. Assim, existe a necessidade de promover a união de ligas com memória de forma sem comprometer as suas propriedades.

O presente estudo, incide sobre a produção de juntas similares de uma liga com memória de forma de Cu-Al-Mn através de soldadura TIG *(Tungsten Inert Gas)*.

As juntas foram avaliadas, de forma a compreender o impacto da soldadura nas propriedades microestruturais e mecânicas das mesmas.

Verificou-se que a liga superelástica de Cu-Al-Mn apresenta boa soldabilidade e não foram detectadas alterações significativas nas propriedades das juntas em comparação com o material base. Este é o primeiro estudo reportado na literatura, que estuda o efeito de um processo de soldadura baseado no arco elétrico para a ligação destes materiais.

Palavras-chave: *Ligas com memória de forma, liga com memória de forma Cu-Al-Mn, soldadura TIG, superelasticidade.*

Abstract

Recently, applications using shape memory alloys (SMAs) have been attracting interest, due to their unique properties. Their application extends to a wide variety of fields, such as automotive, aerospace, biomedical and civil engineering industries.

Among the existing classes of shape memory alloys, NiTi is the most studied one. However, Cu-based SMAs are emerging as potential substitutes of NiTi, due to their lower cost and potential for application in damping devices.

The development of joining technologies is of major interest, because it allows the growth of potential applications of any engineering alloy. Thus, the necessity of studying the joining of SMAs without compromising their properties.

This study focused on the production of similar Cu-Al-Mn joints by gas tungsten arc welding. The microstructure and tensile properties were evaluated to understand the effects of welding on the microstructural and mechanical properties of the welded joints.

The superelastic Cu-Al-Mn presented good weldability and no significant changes of the overall tensile properties of the welded specimens were observed, when compared to the base material. This is the first reported study regarding the effects of welding on Cu-based shape memory alloys, using an arc-based source.

Keyworks: *Shape memory alloys, Cu-Al-Mn shape memory alloys, gas tungsten arc welding, superelasticity.*

Contents

List of Figures

List of Tables

Abbreviations and symbols

A	Austenite
A_f	Austenite transformation finishing temperature
A_s	Austenite transformation starting temperature
AC	Alternating Current
BM	Base Material
d	Grain size
D	Wire diameter
DC	Direct Current
DCEN	Direct Current Electrode Negative
DCEP	Direct Current Electrode Positive
DSC	Differential Scanning Calorimetry
EBSD	Electron Backscatter Diffraction
EDS	Energy Dispersive Spectroscopy
FZ	Fusion Zone
GTAW	Gas Tungsten Arc Welding
HAZ	Heat Affected Zone
HI	Heat Input
I	Welding current
M	Martensite
M_f	Martensite transformation finishing temperature
M_s	Martensite transformation starting temperature
s	Welding speed
SE	Superelasticity
SEM	Scanning Electron Microscopy
SMA	Shape Memory Alloy
SME	Shape Memory Effect
SMM	Shape Memory Material
t	Sheet thickness
TIG	Tungsten Inert Gas
U	Arc Voltage
UTS	Ultimate Tensile Strength
η	Heat transfer efficiency

σ_{A_f}	Stress level at which the stress induced transformation from austenite to martensite finishes
σ_{A_s}	Minimum stress level to start inducing the transformation from martensite to austenite
σ_{M_f}	Stress level at which the reverse stress induced transformation from martensite to austenite finishes
σ_{M_s}	Minimum stress level to start inducing the transformation from austenite to martensite

1

Introduction

1.1 Motivation

Over the past decades, applications using shape memory alloys (SMAs) have been attracting interest, due to the unique characteristics of this class of materials. Their application extends to a wide variety of fields, such as automotive, aerospace, naval and biomedical sectors.

The assessment of the weldability of SMAs is of major interest, because it allows the possibility of obtaining complex structures or the combination of these materials to other engineering ones. Among the existing classes of shape memory alloys, NiTi is the most studied one. However, Cu-based SMAs have been emerging as candidates to replace NiTi, owing to their lower production costs and high damping capacity.

Previous works revealed that laser welding of a Cu-Al-Mn shape memory alloy did not result in any significant deterioration of the overall tensile properties of the welded specimens, with the Cu-based SMA presenting excellent weldability. Furthermore, other studies have also reported that gas tungsten arc welding (GTAW) has the potential to promote joining of this class of alloys and can be employed specially in applications where larger thicknesses are required, since it can generate deeper welds. Additionally, GTAW is significantly less expensive than laser welding. Thus, this study concerns gas tungsten arc welding of a Cu-Al-Mn shape memory alloy, since no previous attempts of using arc-based sources to weld any Cu-based SMAs have been reported.

1.2 Objectives

The present study aims to investigate the feasibility of producing similar Cu-Al-Mn joints using gas tungsten arc welding process. For this, a dedicated welding equipment was designed, namely an orbital welding prototype.

The main scope of this study comprised the production of full penetrating, defect-free welds in Cu-Al-Mn rods, for which different process parameters were tested. Also, structural and mechanical characterization techniques were used to evaluate the welded specimens.

1.3 Document structure

This thesis is organized in five chapters as follows:

- Chapter 1: details the motivation and objectives for this study.
- Chapter 2: contextualizes the study, by presenting the literature review of the existing knowledge regarding Cu-based SMAs.
- Chapter 3: describes the materials, equipment and characterization techniques used throughout this work, along with the experimental procedure adopted. The welding equipment characteristics are included.
- Chapter 4: presents and discusses the results of this study, organized according to the characterization techniques performed.
- Chapter 5: the main conclusions and proposals for future developments are given.

2

Literature Review

2.1 Shape Memory Alloys

Shape memory alloys (SMAs) are a unique class of shape memory materials (SMMs), that present two peculiar and attractive properties: shape memory effect (SME) and superelasticity (SE).

The shape memory effect is a distinct property of certain alloys that exhibit a reversible martensitic transformation, detailed later in this chapter, which was possibly the most studied metallurgical phenomenon during the early 1900s, and first established as an irreversible process. The concept of reversible transformation of martensite was presented in 1949 by Kurdjumov and Khandros, and was based on experimental observations of the thermally reversible martensitic structure in Cu-Zn and Cu-Al alloys, being later demonstrated in other alloys [1,2]

The finding of the SME can be traced back to 1932, being first discovered in an Au-47.5Cd (at.%) alloy by Chang and Read [3]. However, the breakthrough for engineering applications was only triggered in 1963, when significant recoverable strain was observed in NiTi alloys, by Buehler et al. [4].

During the 1970s, several biomedical applications using NiTi emerged, but it was not until the 1990s that relevant NiTi applications had commercial impact.

Nowadays, the demand for shape memory alloys has increased and they can be found in a wide variety of industrial fields, and are commercially desired specially for sensing and actuation applications, and as energy absorbing and damping materials [1,5].

Amongst the existing SMAs, NiTi-based, Cu-based and Fe-based alloys present the most significant commercial importance. NiTi is the most studied shape memory alloy, not just because of its functional properties, but also because it presents high strength and ductility [6], although Cu-based SMAs have the advantage of being more cost effective and having good workability during thermo-mechanical processing [5]. Furthermore, these alloys have been experiencing an increase in their mechanical properties due to a better control of the microstructure , such as grain size and texture, during their production [7].

2.1.1 Phase Transformation in Shape Memory Alloys

As previously mentioned, both the shape memory effect and superelasticity presented by these alloys, are due to a reversible martensitic transformation.

SMAs have typically two phases, each with a different crystal structure and consequently different properties: a low temperature one, known as martensite (M), and a high temperature one, known as austenite (A) [8]. In these alloys, each martensitic crystal has a given different orientation, called variant. The assembly of martensitic variants can exist in two forms: twinned martensite, which is formed by a combination of self-accommodated martensitic variants to keep the overall shape when martensite is thermally induced, and detwinned martensite in which a specific variant is dominant in the system, usually as a result of an applied external load [1,8]. The schematic of the crystal structure of twinned martensite and austenite for a shape memory alloy and the transformation between them is represented in Figure 1.
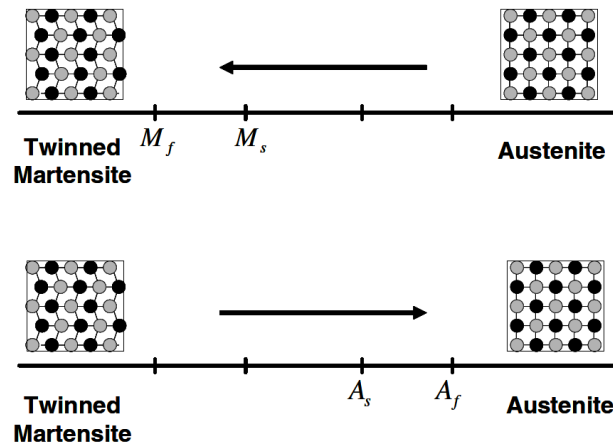
Figure 1 - Temperature-induced phase transformation of an SMA without mechanical loading [1].

Thermo-responsive shape memory alloys present four characteristic temperatures associated with the phase transformation, namely austenite start temperature (A_s), austenite finish temperature (A_f), martensite start temperature (M_s) and martensite finish temperature (M_f).

Without any load applied, when the temperature is lowered from the high temperature austenitic phase, the martensitic transformation begins at M_s. At that temperature, austenite begins to transform to twinned martensite and the transformation finishes when the M_f temperature is reached. At this point, the material is entirely twinned martensite. If the temperature is raised from the low temperature martensitic phase, the martensite becomes unstable and the reverse martensitic transformation begins at A_s and finishes at A_f, fully reverting to the parent phase.

Martensitic transformations, as those that take place in shape memory alloys, are diffusionless transformations, that is the composition of the parent and low temperature phases are kept. When

such transformations occur only by effect of temperature, the macroscopic shape change is negligible [8].

2.1.2 Shape Memory Effect

If a deformation is imposed to the material in the martensitic phase, it is possible to detwin the martensite by reorienting a certain number of variants. The detwinning process results in a macroscopic shape change, where the deformed configuration will be retained by the material, even after the load is released, provided that it remains in the temperature range where martensite is the stable phase. It is possible to recover the original shape when the material is heated above the A_f temperature. When the A_s temperature is surpassed, the shape memory effect starts to occur. In other words, the material starts to recover the previously imposed deformation, leading to the complete recovery of its original shape when the A_f temperature is reached. Further cooling back to the martensite domain, will occur with no significant macroscopic shape change of the material [1,8]. Figure 2 schematically represents both superelasticity and shape memory effect in a stress-strain-temperature diagram.
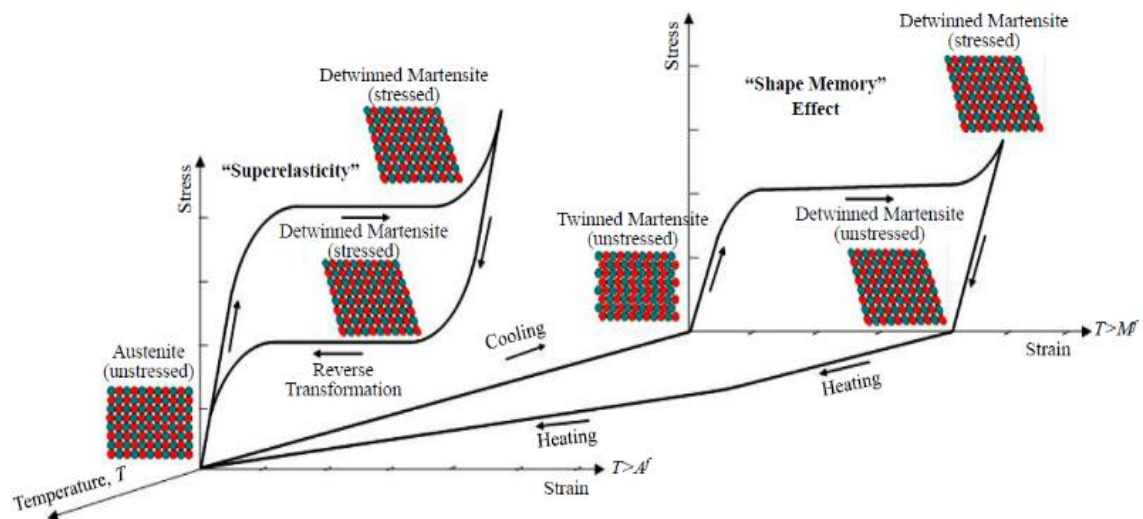
Figure 2 - Stress-strain-temperature plot exhibiting superelasticity and shape memory effect [9].

2.1.3 Superelasticy

While at low temperatures SMAs exhibit the shape memory effect, at high temperatures recovery can be achieved instantly upon releasing the applied load, just like rubber band. This is called superelasticity [5].

The superelastic behaviour of SMAs is associated with a stress-induced transformation. Superelasticity occurs by the application of stress when the material is in the temperature range of thermally stable austenite, and then progresses under an applied load to a state at which detwinned martensite is stable, finally returning to the austenitic phase when returned to zero stress state, provided that the imposed deformation does not exceed the stress to induce slip. To better illustrate this behaviour, the path depicted in Figure 3 is taken into consideration (A → B → C → D → E → F → A).
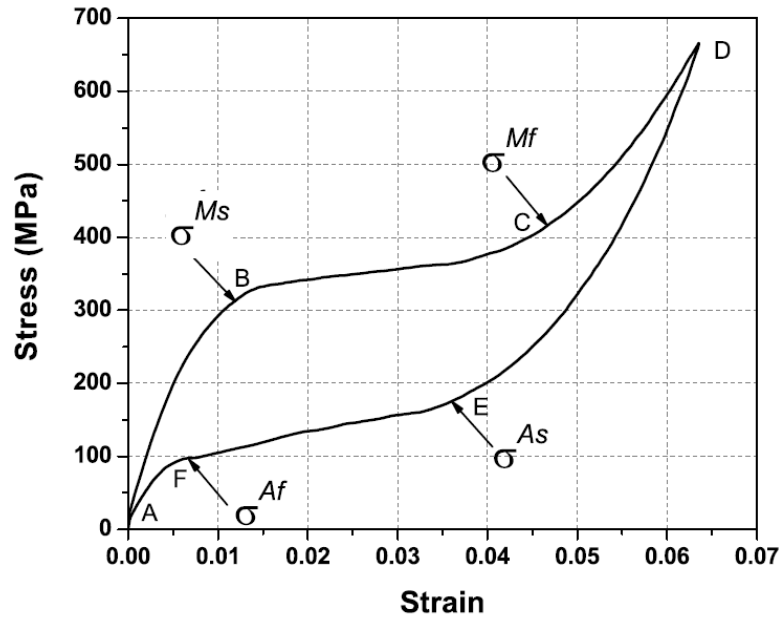
Figure 3 - Typical superelastic behaviour of a shape memory alloy [1].

Firstly, when a mechanical load is applied there is elastic deformation of austenite (A→ B). At B, for a given stress, σ_{Ms}, the martensitic transformation starts to occur. The transformation continues (B → C), to the stress level (σ_{Mf}) where the loading path intersects the M_f transformation surface. When σ_{Mf} stress is reached, the material is fully martensitic. From C to D there is the elastic loading of detwinned martensite. From D to E the martensite elastically unloads. At point E, for a σ_{As} stress level the martensite to austenite transformation starts to occur and proceeds until it is finished (at point F). Complete removal of the imposed stress allows for the elastic unloading of austenite (along the path F→A) [1,10].

In addition to the shape memory effect and superelasticity, there is another functional property exhibited by these materials: the two-way shape memory effect. This behaviour is not often a standard feature of commercial SMAs. It is achieved after a training process that consists of applying a large number of repeated thermomechanical cycles at high and low temperatures. This procedure will cause the material to remember a given geometrical shape at those temperatures and only by thermal action it is possible to obtain a change in the shape of the material [1,10].

2.1.4 Cu-based Shape Memory Alloys

Among the different available Cu-based shape memory alloys, a Cu-Al-Mn alloy is going to be studied in the present work. Hence the fact that this section is focused on this particular class of alloys.

Although a large number of shape memory alloys has been discovered, most are Cu-based. In particular, the Cu-17Al-11.4Mn (at.%) alloy exhibits the highest performing superelastic properties among Cu-based SMAs and has mechanical properties that are similar to those of NiTi, but has better thermal and electrical properties, and can exceed the recoverable strain achieved by NiTi [11,12]. These advantages have recently motivated numerous investigations into these alloys. The Cu–Al binary system is the most important of the Cu-based SMAs because of its superior properties, namely excellent ductility [13,14].

The metastable β-phase orders during cooling, and for a certain range of compositions ($(Cu_{0.75}Al_{0.25})_{1-x}Mn_x$, being $0 \leq x \leq 0.09$ and $Cu_3Al_{1-x}Mn_{2x}$, with $0 \leq x \leq 0.22$), at lower temperatures experiences a first-order, diffusionless, structural transition into a closer packed phase [10,15]. This is the basis of the martensitic transformation in Cu-based alloys.

However, problems may emerge for Cu-based alloys with high Al content with the β_2 or the β_1 ordered structure. Cu-based SMAs such as Cu–Al–Ni and Cu–Zn–Al with a polycrystalline structure are too brittle to be sufficiently cold worked and have very low fatigue strength. Furthermore, the low ductility of Cu-based shape memory alloys, is usually attributed to large grain size, high degree of elastic anisotropy and grain boundary segregation of impurities. This can be considered a setback in terms of practical applications, although several attempts to improve the ductility of these alloys by grain refining have been made [10,16].

The effect of the Al content on the shape memory effect and superelastic properties was studied by Kainuma et al. [17] in 1995. The authors first reported, that Cu–Al–Mn alloys with low Al composition (<17 at. %), demonstrated an exceptional ductility, as well as stable superelastic properties and excellent cold-workability. From that point onwards, special attention was dedicated to these materials.

The addition of Mn to the binary Cu-Al alloy was found to stabilize the body centered cubic β-phase, widen the single-phase region to lower Al compositions and lower temperatures, and improve the ductility of the low Al content alloys by decreasing the degree of order of the parent phase. Previous studies on the Cu-17Al-11.4Mn alloy have shown that the superelastic properties of these wires are extremely dependent on the relative grain size to wire diameter ratio, d/D, where d is the grain size and D the wire diameter. Higher d/D leads to a higher strain recovery by superelasticity, due to the decrease of the grain constraint by the surrounding grain boundaries; lower d/D increases the critical stress for the martensitic transformation and reduces the extension

of the superelastic plateau thus, the ability to recover imposed deformation by superelasticity decreases [18–20].

The phase diagram for a Cu-Al-Mn alloy is represented in Figure 4. It can be observed that the transition temperatures of order-disorder transitions β (A2) $\rightarrow \beta_2$ (B2) and β_2 (B2) $\rightarrow \beta_1$ (L2$_1$) severely decrease with the Al content. Increasing either the Mn or the Al content of the alloy decreases the transformation temperatures, with a greater sensitivity to modifications in the Mn content. The α-phase, which can also appear in these shape memory alloys, has a face centered cubic structure. In these complex Cu–Al–Mn systems, three different low phase temperature (martensite) structures can occur, depending on the composition of the Cu-Al-Mn alloy: α'_1 (3R structure) forms with low Al content, β'_1 (18R structure) forms in an intermediate range and the γ'_1 (2H structure) phase is predominant in higher Al content ranges [10,16].
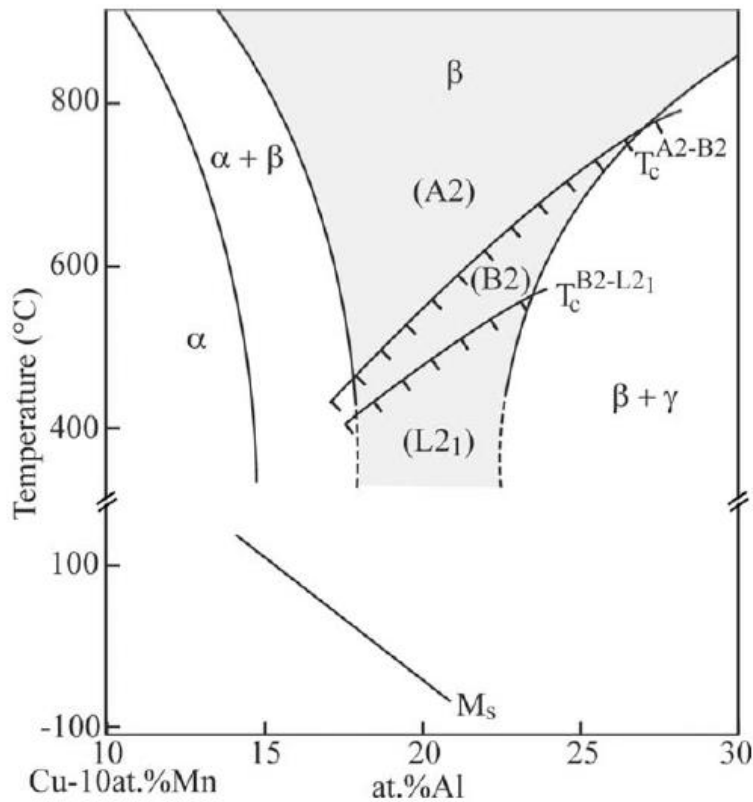
Figure 4 – Cu-Al-Mn phase diagram. Vertical section of the Cu-Al-10at.%Mn system including martensitic transformation starting temperature [20].

2.1.5 Applications

Due to their unique characteristics, NiTi and Cu-based shape memory alloys, which can exhibit both shape memory effect and superelasticity, and can have high tensile strength and damping capacity are attracting attention. These particular properties make them suitable candidates for

applications in multiple fields, for instance in the biomedical, aerospace and automotive industries, and especially in civil engineering in structural vibration control applications [1,11,12,16,21–25]. Although NiTi is currently the most used SMA, Cu-based shape memory alloys are arising as potential alternatives, and they are being considered as a replacement of NiTi in vibrational and damping applications, like seismic devices [12,23,24].

Since conventional steel tension braces often present degraded stiffness and strength under cycling loading, Araki et al. [12] studied the possibility of using Cu-Al-Mn superelastic alloys as energy dissipating and recentering elements, in tension braces in steel frame structures as partial replacement of steel bars, depicted in Figure 5. Both static and dynamic tests showed the effectiveness of the Cu–Al–Mn superelastic alloys brace system in controlling the behaviour of the steel frame, presenting a more stable response under cyclic loading when compared to steel. The results also showed their negligible rate dependency to high-frequency excitations, demonstrating that the use of Cu–Al–Mn alloys in seismic applications has great potential [14,23].
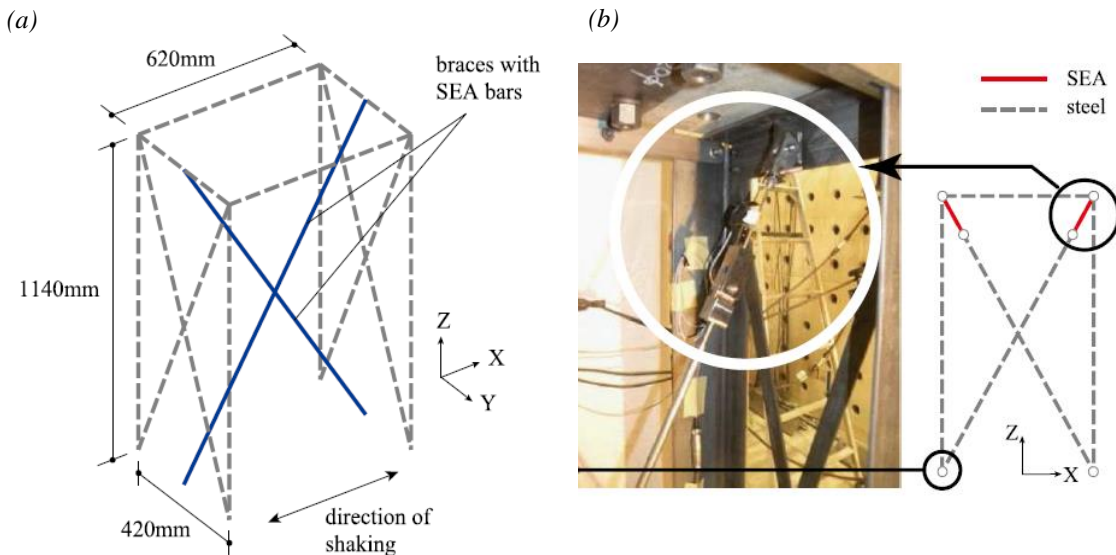
Figure 5 – (a) Schematic view of the steel frame specimen. (b) Detail of the top pin joints in the tension braces [12]

In the medical field, the application of Cu-Al-Mn based SMAs as guidewires was introduced, making them unique guidewires, because of their functionally graded properties. These graded properties attained by microstructural control cannot be achieved in guidewires made of NiTi and stainless steels. Cu–Al–Mn-based SMAs can be produced not just as sheets and wires, but also as tubes and thin foils, making their application less limited [16]. Also in the field of biomedical applications, the superelastic Cu-17Al-11Mn SMA is a primary candidate and is currently used for ingrown nail correction as it does not present risks to the human health [14].

2.2 Joining of Shape Memory Alloys

A wider application of shape memory alloys in multiple industrial sectors is inhibited by the difficulties in their processing. SMAs have poor workability when it comes to conventional machining processes [26], and their increasing importance makes the development of suitable joining techniques in order to obtain complex shaped components crucial.

Welding of shape memory alloys presents challenges when compared to welding performed on other alloys because, opposite to most materials, SMAs properties are heavily dependent on the chemical composition, microstructure and transformation temperatures, so it must be ensured that, after joining, the superelastic and shape memory effect properties are maintained [27].

The number of studies reported in the literature, regarding welding techniques of SMAs, have shown substantial growth in the last few decades. Since this study concerns gas tungsten arc welding of a Cu-Al-Mn shape memory alloy, this chapter presents this process and studies regarding welding of Cu-based SMAs. Concerning specifically to gas tungsten arc welding, no previous attempts of welding any Cu-based shape memory alloys using this process have been reported.

2.2.1 Gas Tungsten Arc Welding

The existence of welding can be traced back to ancient times, but it was not until the 20th century, when important scientific and technological discoveries occurred, that a wide variety of welding processes commence their commercial use. Amongst these discoveries, it is the electric arc in 1801.

The possibility of using inert gases as a shielding atmosphere for the welding arc and weld pool was first investigated in the 1920s by H. M. Hobart [28] and P. K. Devers [29]. However, it was only in the beginning of World War II that there was the necessity for further developments, when better shielding was required for joining reactive metals, such as aluminum and magnesium [30]. The process was perfected by R. Meredith and patented in 1942, being originally named *Heliarc welding* [31]. This led to the first commercial development of gas tungsten arc welding equipment.

Gas tungsten arc welding (GTAW) commonly referred to as tungsten inert gas (TIG), is an electric arc-based welding process, that uses the heat generated by an electric arc established between a non-consumable tungsten electrode and the workpiece to melt the base material (BM) and promote the formation of a weld pool. This process is used with shielding gas (typically Argon or Helium) in order to provide an inert atmosphere that protects the weld pool from air contamination. The electrode is made of Tungsten, due to its high melting temperature and thermal emissivity [30,32].

Gas tungsten arc welding can also be employed with or without the addition of filler metal, usually in the form of wire. Autogenous GTAW (without filler metal) is applied in thin sections with square edges, up to 2 mm, whereas for thicker sections, V and X type edge preparations and the addition of filler metal is required [33].

The GTAW process is illustrated in Figure 6 and the four basic components of all gas tungsten arc welding setups are a torch, the electrode, a welding power source and shielding gas.
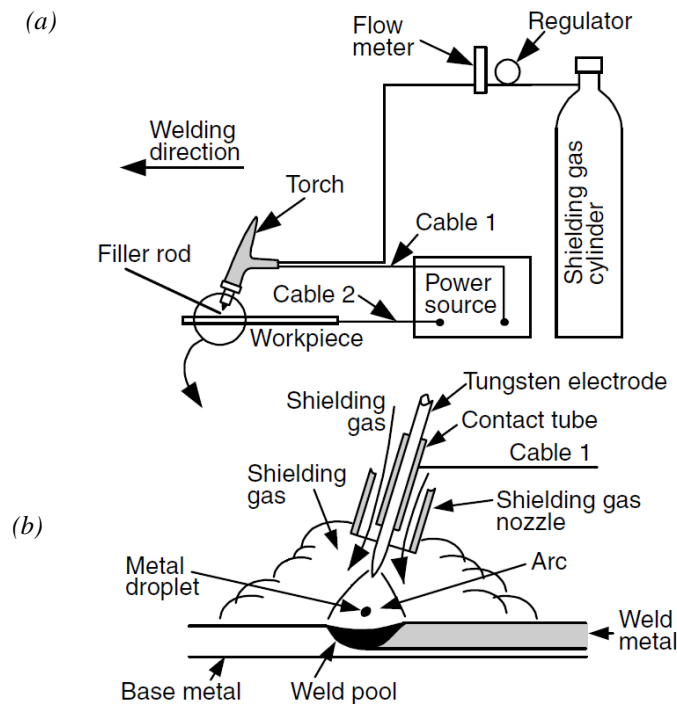
Figure 6 - Gas tungsten arc welding: (a) overall process; (b) welding area. Adapted from [34].

The main parameters of this process are: the welding current, welding speed, arc length and shielding gas. Weld bead configuration, welding speed and weld quality are directly influenced by the current type. Gas tungsten arc welding can be used with direct current (DC) or alternating current (AC), being the choice largely dependent on the material to be welded. Using direct current, the tungsten electrode can be connected to either the negative or the positive terminal of the power source. Direct current electrode negative (DCEN) is the most common configuration in GTAW. With that polarity, when the arc is established, electrons flow from the electrode to the workpiece. In DCEN most heat is concentrated on the workpiece, leading to deeper weld penetration and allowing for higher welding speed [30,33]. In direct current electrode positive (DCEP), the tungsten electrode is connected to the positive terminal and the direction of electrons and positive ions flow are reversed. In this case, most of the heat is concentrated on the electrode, which produces degradation of the tip, consequently the workpiece has less heat resulting in a shallow penetration of the weld bead. DCEP may be of interest in welding aluminum alloys

because of the cathodic cleaning action created at the surface of the workpiece, that is, the breaking and removal of the refractory aluminum oxide layer [30,33]. However, alternating current suffers periodic reversal in polarity from electrode positive to electrode negative, allowing the combination of both the advantages of DCEN and DCEP per cycle, that is deep penetration and workpiece cleaning action. Thus, it avoids the disadvantages of both, making it more suitable to weld aluminum and magnesium alloys.

The characteristics of each configuration are presented and summarized in Figure 7.
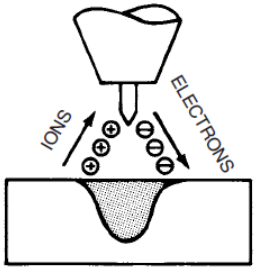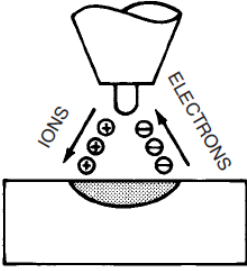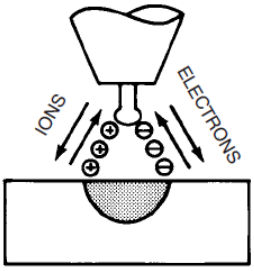
CURRENT TYPE	DCEN	DCEP	AC (BALANCED)
ELECTRODE POLARITY	NEGATIVE	POSITIVE	
ELECTRON AND ION FLOW			
PENETRATION CHARACTERISTICS			
OXIDE CLEANING ACTION	NO	YES	YES—ONCE EVERY HALF CYCLE
HEAT BALANCE IN THE ARC (APPROX.)	70% AT WORK END 30% AT ELECTRODE END	70% AT WORK END 30% AT ELECTRODE END	70% AT WORK END 30% AT ELECTRODE END
PENETRATION	DEEP; NARROW	SHALLOW; WIDE	MEDIUM
ELECTRODE CAPACITY	EXCELLENT e.g., 3.2 mm (1/8 in.) 400 A	POOR e.g., 6.4 mm (1/4 in.) 120 A	GOOD e.g., 3.2 mm (1/8 in.) 225 A

Figure 7 - Characteristics of the three different polarities in GTAW [30].

The welding speed affects weld bead configuration, mainly the width, but also penetration of a gas tungsten arc weld. For the same current and voltage, increasing welding speed leads to a reduction of the heat input [33].

The heat input (HI) is a measure of the energy transferred from the arc to the workpiece per unit length of a weld, and is calculated as the ratio between the welding power and the welding speed, as follows:

$$HI = \frac{U.I}{s} \times \eta \qquad [J/mm]$$

Where, U is the arc voltage [V], I is the welding current [A] and s is the welding speed [mm/s]. The efficiency in the GTAW process is approximately 0.75.

GTAW is a very controllable and precise process, extensively utilized in precision welding, particularly in thin components of stainless steel, aluminum, magnesium or titanium alloys, and offers multiple advantages, namely: it allows a precise control of the heat addition, limiting to some extent the dimensions of the thermally affected zones; it is capable of producing consistent

beads of superior quality at high speeds, with low distortion and spatter-free; it is easy to obtain a stable arc even for small current intensities; welds can be done in any position; it allows the joining of materials with a wide variety of thicknesses [8,30,33,35,36].

Although GTAW presents several benefits, the heat source is not as focused as in laser welding. Therefore, when both techniques are directly compared it is observed that in GTAW welds the heat affected zone (HAZ) and fusion zone (FZ) have a higher extension, which may lead to a loss in the shape memory and superelastic characteristics.

2.2.2 Gas Tungsten Arc Welding of Shape Memory Alloys

Despite the extensive range of welding techniques employed in shape memory alloys, laser welding is, by far, the most widely used joining process, due to its particular characteristics such as low heat input, high energy density, reduced extension of the heat affected zone and fusion zone [8].

Limited information regarding the use of arc welding techniques can be found, since arc welding processes regularly produce welds with extended heat affected zones, which are not desired in most cases.

Gas tungsten arc welding was the first welding process tested in similar NiTi joints in 1961 [4], where, although no mechanical analysis was performed, the production of defect- and porosity-free joints was accomplished. However, due to insufficient protection of the molten pool during the weld, interstitial phases were observed. In 1996, Ikai et al. [37], resumed this process and successfully welded NiTi wires with different transformation temperatures, though significant degradation of the mechanical properties of the joints was observed. More recently, Oliveira et al. [36] performed a study where the welding of 1.5 mm NiTi plates in butt joint configuration using GTAW was successfully accomplished. The transformation temperatures of the fusion zone showed a slight decrease in comparison to the base material, due to Ti oxidation. The uniaxial tensile tests results exhibited an elongation to rupture of 20% and a superelastic plateau of 30 MPa, below that of the base material. The superelastic behaviour of the welds was confirmed by cycling tests performed at 4, 8 and 12% of strain for 600 cycles. The shape-memory effect was also preserved after welding, and even after 600 cycles. This work shows that although laser welding is often stated as the most suitable process for joining NiTi, GTAW also has the capability of promoting such joining, especially for industrial applications where thicknesses above 1 mm are required.

Another work regarding the use of GTAW for NiTi, was published by Fox et al. [35], where actuators were manufactured by joining NiTi and 304 stainless steel tubes of 9.53 mm in diameter through orbital welding. The results demonstrated that laser welding was more appropriated for

shallow welds in thin walled tubes, in opposition to GTAW where the weld was performed in a single pass, resulting in a HAZ five times larger when compared to the laser one.

2.2.3 Welding of Cu-based Shape Memory Alloys

Reported studies concerning welding of shape memory alloys are mainly dedicated to NiTi, although recent research has focused on the weldability of Cu-based SMAs.

Oliveira et al. [14] presented the first study on the effects of laser welding on the mechanical properties of superelastic Cu-Al-Mn wires. No significant detrimental effect to the overall tensile properties of the welded specimens was observed when compared to the base material, with fracture always taking place far away from the welds. After mechanical cycling, the welded wire demonstrated higher irrecoverable strain compared to the base material, due to the fine-grained structure of the fusion zone, whereas the base material kept its bamboo-like microstructure. Thus, concluding that the Cu-Al-Mn alloy has excellent weldability, which may lead to an increase in its use.

Post-weld processing is often performed to improve the mechanical properties of welded joints. The effect of post-weld laser heat treatment was investigated in the improvement of the mechanical properties and damping capacity of a laser welded superelastic Cu-17Al-11.4Mn (at.%) alloy [19]. It was concluded that the tensile strength of the post-weld laser processed alloy increased almost to the double of the as-welded material and base material, while the capability to absorb energy increased up to 1.7 times.

Oliveira et al. [38] also published a work regarding another Cu-Al-based SMA. In this case, laser welding was performed on the single crystal-like Cu-11.5Al-0.5Be (wt.%) shape memory alloy. Defect-free joints were obtained, with the same crystallographic texture as the base material. Similarly, the superelastic behaviour of the welded joints was preserved, revealing the potential to employ this SMA in applications requiring high damping capacities, because of their large energy absorption capacities. There is also a study concerning the effect of laser welding on the microstructure and mechanical properties of Cu-Zn open cell foams, where the laser weldability of the open cell foams was successfully confirmed, presenting reasonable mechanical properties and crack free welded beads [39].

Production of dissimilar joints is also desirable, because it takes advantage of the properties presented by two distinct materials, which is fundamental for the development of new applications. Nonetheless, dissimilar joining can present significant difficulties due to the various metallurgical and thermo-physical problems that can emerge. Oliveira et al. [40] presented a work where dissimilar laser welding of NiTi and Cu-Al-Mn shape memory alloy was performed. The study showed the obtainment of defect-free joints and the preservation of the superelastic

properties after welding, despite the unfavourable microstructure of the fusion zone which led to an irrecoverable strain of 2% (for a maximum applied strain of 5%).

2.3 Conclusions

Shape memory alloys are now increasingly being used in many applications because of their unique properties. Amongst these alloys, Cu-based SMAs have the broadest application prospect besides that of NiTi alloys, due to their lower production cost and by exhibiting good functional properties. These alloys are currently being studied for potential applications as damping systems in seismic devices.

Joining techniques are often required to obtain complex geometries to increase the variety of potential applications. Therefore, determining the weldability of a material will allow the production of these complex shapes.

Multiple fields would benefit from dissimilar joining of SMAs to current alloys used in those areas. Thus, preliminary studies to investigate the weldability of the Cu–based alloys in similar joints are necessary.

The main scope of this work is focused in the production and testing of Cu-Al-Mn similar joints. The mechanical properties are assessed, so that future components can be successfully designed.

3

Experimental Procedure

This section presents the materials and equipment used throughout this study, as well as the adjustments introduced in the weld source. The experimental approach adopted to perform similar Cu-Al-Mn joints and the characterization techniques used to assess the quality of the welds are described.

3.1 Material Characterization

The Cu-17Al-11.4Mn (at.%) alloy was prepared by induction melting under an Argon atmosphere, in order to form an ingot. To obtain the Ø6 mm rods, the ingot was hot forged and cold drawn. To attain the superelastic properties, the rods were subjected to a solution treatment at 900˚C, subsequently quenched in water, and were then aged at 200ºC, to stabilize the martensitic transformation temperatures as described in [20].

Prior to welding, the surface oxide layer was removed with SiC paper and the rods were cleaned with ethanol, so that any impurities that could interfere with the weld would be eliminated.

Table 1 summarizes the mechanical properties of the material used.

Commercial pure Argon was used as shielding gas to avoid oxidation of the material. Table 2 depicts the chemical composition of this gas.

Table 1 - Mechanical properties of superelastic Cu-17Al-11Mn.

Material	Young's modulus [GPa]	Onset for stress induced transformation [MPa]	Recovery strain [%]	Work-hardening rate [GPa]	Tensile elongation [%]
Cu-17Al-11Mn	≈20 [24]	≈100 to 250 [20]	Up to 12% [24]	≈3.4 to 4.2 [20]	Up to 18 [24]

Table 2 - Shielding gas composition.

Alphagaz 2	Ar	H_2O	O_2	CnHm	CO	CO_2	H_2
	≥ 99.9999%	≤ 0.1 ppm	≤ 0.1 ppm	≤ 0.1 ppm	≤ 0.1 ppm	≤ 0.1 ppm	≤ 0.1 ppm

3.2 Equipment

In this sub-section the description of the development of an orbital welding system that allowed the production of welds in the Ø6 mm rods is presented.

3.2.1 Welding Equipment

A welding machine from *TELWIN*, model *Technology TIG 182 AC/DC-HF/LIFT* (Figure 10), was used. The main characteristics of the equipment are listed in Table 3.

Table 3 - TELWIN Technology TIG 182 AC/DC-HF/LIFT Technical data [41].

Single Phase Mains Voltage	230 V
Mains Frequency	50 / 60 Hz
Current Range	5 – 160 A
Max Current (at 40°C)	160 A – 20%
Max. No Load Voltage	94 V
Max Absorbed Current	29 A
Max Absorbed Power	4.3 kW
Mains Fuse	16 A
Efficiency	75 %
Power Factor ($cos\varphi$)	0.7

3.2.2 Trigger System

To guarantee repeatability of the conditions and parameters, such as the distance of the tungsten electrode to the welding rod, modifications were performed to allow the torch to be remotely activated, avoiding disturbances. Thus, the welding torch was fixed to a 30x30 mm *Bosch Rexroth's* profile with a 3D printed support and was triggered by adding a relay, connected to an ON/OFF switch, activated through a digital port in the *Arduino*, depicted in Figure 10 and schematically shown in Figure 8.
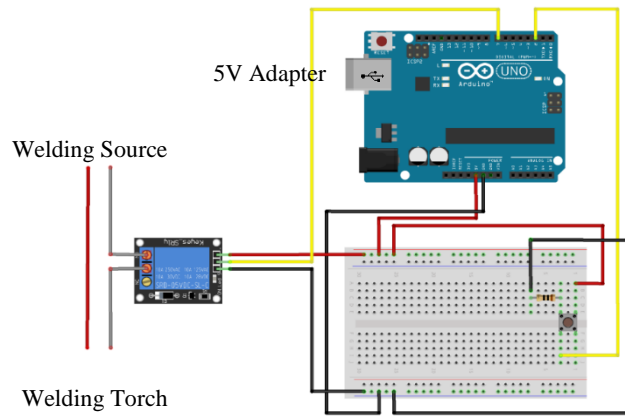
Figure 8 - Trigger system. Relay and ON/OFF switch circuit schematics.

3.2.3 Motion System

To guarantee rotational motion and process automation, a stepper motor was used. This type of motor is commonly employed in applications requiring precise positioning at low speeds, since they move in precise repeatable steps, allowing good control of the rotational speed. The selected model was the *NEMA 17 Bipolar Motor*, that has a 1.8° step angle (200 steps/revolution) and was controlled by a *DRV8880 Stepper Motor Driver Carrier*. For the stepper motor to work a power supply is also necessary, in this work, a 9V / 3A adapter was used. The motion system is depicted in Figure 10 and schematically shown in Figure 9.
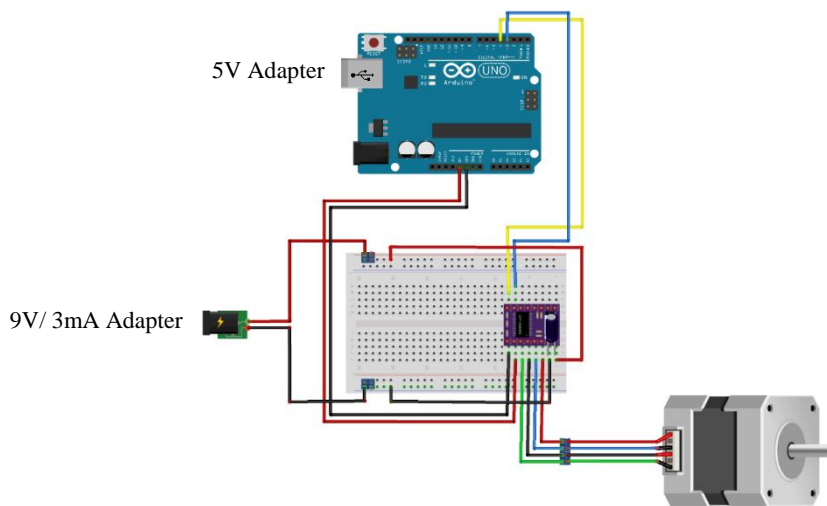
Figure 9 - Motion system. Stepper motor circuit schematics.
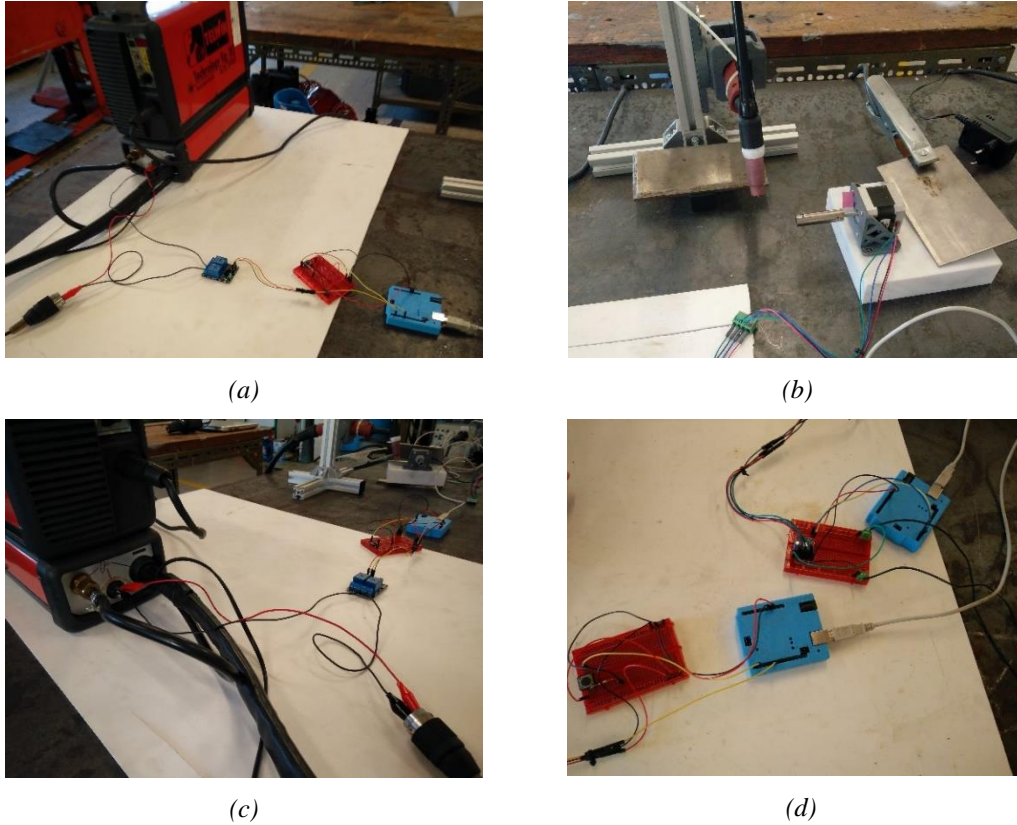
Figure 10 - Welding equipment. Welding machine and trigger system (a), (c); motion system and welding torch (b); trigger and motion system (d).

3.3 Experimental Approach

The similar Cu-Al-Mn joints were attained by varying the following welding parameters: welding speed, welding duration and welding current. Since this is the first study on arc welding of these materials, bead-on-plate welds were produced. This reduces the variability of joint-fit up, allowing the focus to be only on the welding parameters. The Argon flow rate was kept constant at 10 l/min which ensured an oxidation-free weld by visual inspection. A thoriated tungsten electrode with Ø2mm was used. Compared to pure tungsten electrodes, these possess better electron emissivity, current-carrying capacity and resistance to contamination, which results in a more stable arc [30].

Tests were performed to determine the optimum welding parameters to obtain full penetrating and defect-free welds, using direct current and straight polarity, which is the most common polarity in GTAW. In gas tungsten arc welding with DCEN, more power is located at the work end of the arc and less at the electrode tip, thus resulting in relatively narrower and deeper welds when compared with DCEP, which is normally used for welding thin sheets of strong oxide-forming materials, where deep penetration is not required [34].

Table 4 - Welding parameters.

Sample	Speed [rpm]	Welding duration [s]	Welding speed [mm/s]	Welding current [A]	Gas flow rate [l/min]	Heat input [J/mm]
#1	15	8	9.4	35	10	31.8
#2	10	11	6.3	40	10	55.4
#3	15	9	9.4	40	10	36.9
#4	12	9	7.5	40	10	46.0
#5	10	11	6.3	40	10	55.4
#6	12	10	7.5	40	10	46.2
#7	12	11	7.5	40	10	46.2
#8	12	11	7.5	42	10	48.8
#9	12	12.5	7.5	40	10	46.2
#10	12	11.5	7.5	40	10	43.5
#11	12	12	7.5	38	10	46.2

After, the welded specimens were characterized as described in the following sub-section.

3.4 Characterization Techniques

3.4.1 Differential Scanning Calorimetry

Differential scanning calorimetry (DSC) was used to characterize the structural transformation temperatures of the Cu-Al-Mn base material. Because DSC analysis requires specimens of reduced dimensions, a precision cutting machine was used to obtain a small part of the base material. A *DSC 204 F1 Phoenix* from *Netzsch* was used, available at the CENIMAT facilities. The temperature range was set between -150 and + 150 ºC, for a heating/cooling rate of 10 K/min.

3.4.2 Optical Microscopy

Microstructural analysis was performed on the welds longitudinal section. The welded samples were cut using a precision cutting machine and mounted in epoxy resin, mechanically polished up to 2500 fine SiC paper and etched in a $FeCl_3$ (10 g) + HCl (25 ml) + H_2O (100 ml) solution. Optical observations were then conducted at CENIMAT, using a *Leica DMI5000 M* optical microscope.

3.4.3 Scanning Electron Microscopy coupled with Energy Dispersive Spectroscopy

Scanning electron microscopy (SEM) was used for fine microstructural characterization of the fusion zone of the joints, as well as for observation of the fracture surfaces of the specimens after uniaxial tensile tests. Furthermore, energy dispersive spectroscopy (EDS) was used to assess the homogeneity of the chemical composition in both the fusion zone and heat affected zone of the welds. These measurements were performed using a *Zeiss Auriga* scanning electron microscope, available at CENIMAT, operating at an acceleration voltage of 17 kV. The samples for microstructural characterization were coated with carbon to improve conductivity.

3.4.4 Electron Backscatter Diffraction

The crystallographic orientation and phases in the fusion zone, heat affected zone and base material of the welded joints were determined by Electron Back-Scattered Diffraction (EBSD) technique. EBSD was performed using a field emission SEM at Tohoku University.

3.4.5 X-Ray Diffraction

X-ray diffraction (XRD) analysis was performed on a welded specimen to identify and characterize the phases present at room temperature. A *Brucker* diffractometer (rotating anode – *XM18H*, Cu-Kα radiation (1.5418 Å), 30 kV/100 mA) with conventional θ/2θ scanning, available at CENIMAT was used. The XRD technique was selected to analyse the fusion zone of the joints, since the weld thermal cycle may alter the existing phases.

3.4.6 Hardness Tests

Vickers hardness measurements were performed along the longitudinal section of the welded specimen, to access the effects of the welding process across the welded joints. A *Mitutoyo HM-112* microhardness tester was used, and a test load of 200 g was applied for 10 seconds. A total of seventeen hardness measurement lines were performed, with indentations distancing 200 μm horizontally and 100 μm vertically, thus evaluating fusion zone, heat affected zone and base material. From these measurements a bidimensional (x, y) hardness map was constructed to evaluate the microhardness changes across the fusion zone up to the base material.

3.4.7 Mechanical Tests

The mechanical properties of the welded specimens, as well as those of the base material for reference use, were determined by uniaxial tensile tests and cycling tests. The tensile tests were performed at room temperature, at CENIMAT, on an *Autograph Shimadzu AG50kNG* machine,

equipped with a load cell type *SFL-50kN AG*. To eliminate potential gripping problems, the cylindrical specimens were machined, being the gauge length of the tested samples, for both base and welded material, 30 mm, as depicted in the technical drawing in Appendix A.

Uniaxial tensile tests were used to determine the ultimate tensile strength (UTS) and the elongation to fracture of the welded samples. Three welded samples were tested, at a displacement rate of 1 mm/min. The fracture stress and strain were determined from the stress-strain curves.

Cycling behaviour of the base material and welded specimens was also accessed. A total of 100 load/unload cycles at a strain of 8% were performed, also at a rate of 1 mm/min. Raw data processing allowed to determine the irrecoverable strain and absorbed energy variation as a function of the number of cycles.

Results and Discussion

The experimental results of this study are presented and discussed throughout this chapter, organized by the characterization techniques used.

4.1 Microstructural Characterization by Differential Scanning Calorimetry

The martensitic transformation starting temperature (M_s) and reverse transformation finishing temperature (A_f) of the base material were determined by differential scanning calorimetry. Figure 11 depicts the DSC curve of the base material sample. Upon heating, only one endothermic peak is observed corresponding to the transformation of martensite into austenite. An identical behaviour is observed upon cooling. The existence of just one exothermic peak upon cooling indicates the transformation from austenite to martensite. At room temperature the base material is fully austenitic. As expected, it can also be observed that the high and low temperature peaks are symmetrical and well-defined [5,42].
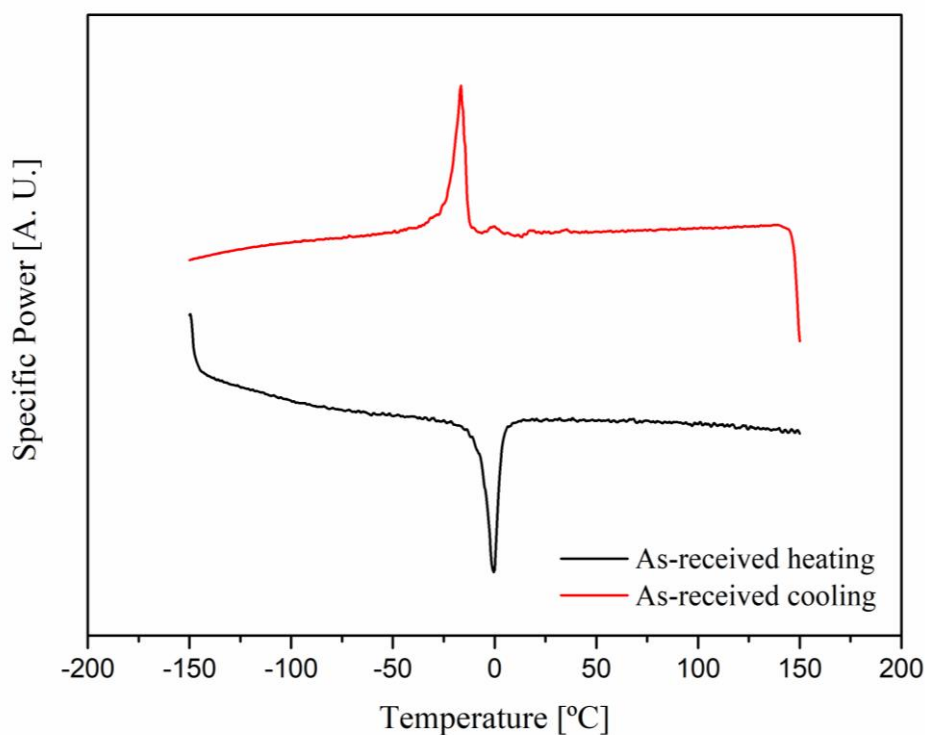

Figure 11 - Differential scanning calorimetry of the base material.

4.2 Microstructural Characterization by Optical Microscopy and Electron Backscatter Diffraction

The first welds produced had the purpose of evaluating process parameters, such as welding speed, welding duration and welding current, with the finality of achieving parameters that allowed the obtainment of full penetration and defect-free welds.

Microstructural observations were carried out on the welded rods (Figure 12) longitudinal section, as depicted in Figure 14.

100 mm
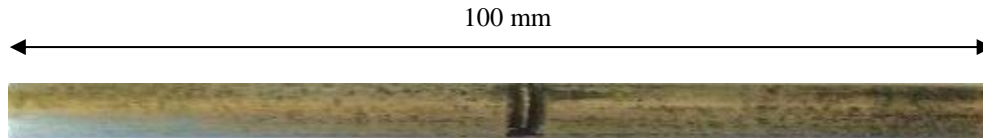
Figure 12 - Welded rod.

Figure 13 presents micrographs of samples #6 and #7 (which welding parameters are described in section 3.3), where only partial penetration was attained, due mainly to insufficient welding duration. From these results, the effects of the welding parameters are visible, and it can be noted that

maintaining, for instance, the welding speed and current constant, varying only welding duration will lead to different weld geometries.
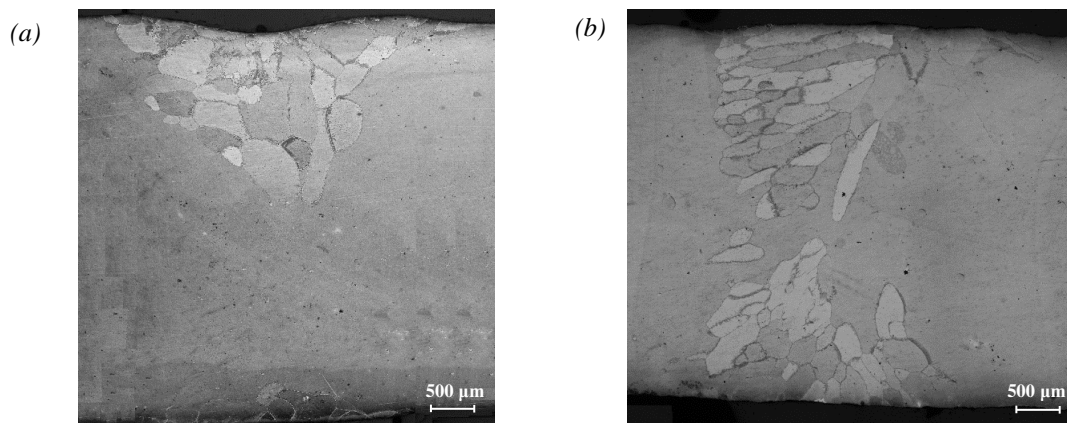
Figure 13 - Optical micrographs of the fusion zone of the welded Cu-Al-Mn alloy. (a) Sample #6; (b) Sample #7.

Welding duration and welding speed are two complementary parameters, since reduced welding speeds together with low welding time will result in welds without full penetration, since the weld will not cover the entire perimeter of the rod. Excessive welding speeds will also only result in partial penetration welds. Lower welding speeds will increase the heat input, and combined with higher welding durations can cause the material to melt completely without forming a joint, which occurred in sample #8.

For a specific set of parameters (sample #11), full penetration of the Cu-Al-Mn specimen was obtained. Figure 14 depicts the welded specimen cross-sectional view, in which the welding zones are identified. Macrographs from the welded specimen are presented in Figure 15. Figure 15 (b) has letters from "a" to "e" identifying a specific region, since each of these regions has a corresponding optical microscopy image, depicted in Figure 17. No welding defects such as pores or cracks were observed within the fusion zone. Microstructural analysis by optical microscopy showed the single crystal base material and revealed that the fusion zone presents a coarse grain structure, with grain size ranging from 70 μm to 1,4 mm. In the fusion zone, a columnar epitaxial grain structure is observed, which results from grain growth starting on pre-existing solid grains of the initial base material on the fusion boundary, where the thermal gradient is more severe [34] and progresses perpendicular to isothermal lines, parallel to the heat flow direction, growing towards the weld centreline where the heat flow decreases. For this specimen, the welded zone does not show symmetry. This maybe because the rods presented a slight warp from their production, which can lead to arc instability. Despite this, full penetration and defect-free joints were obtained with the optimized welding parameters.
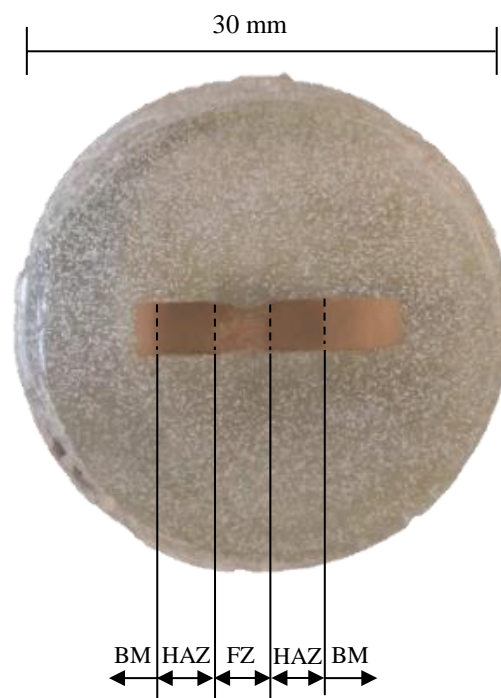
Figure 14 - Longitudinal section of the welded specimen.
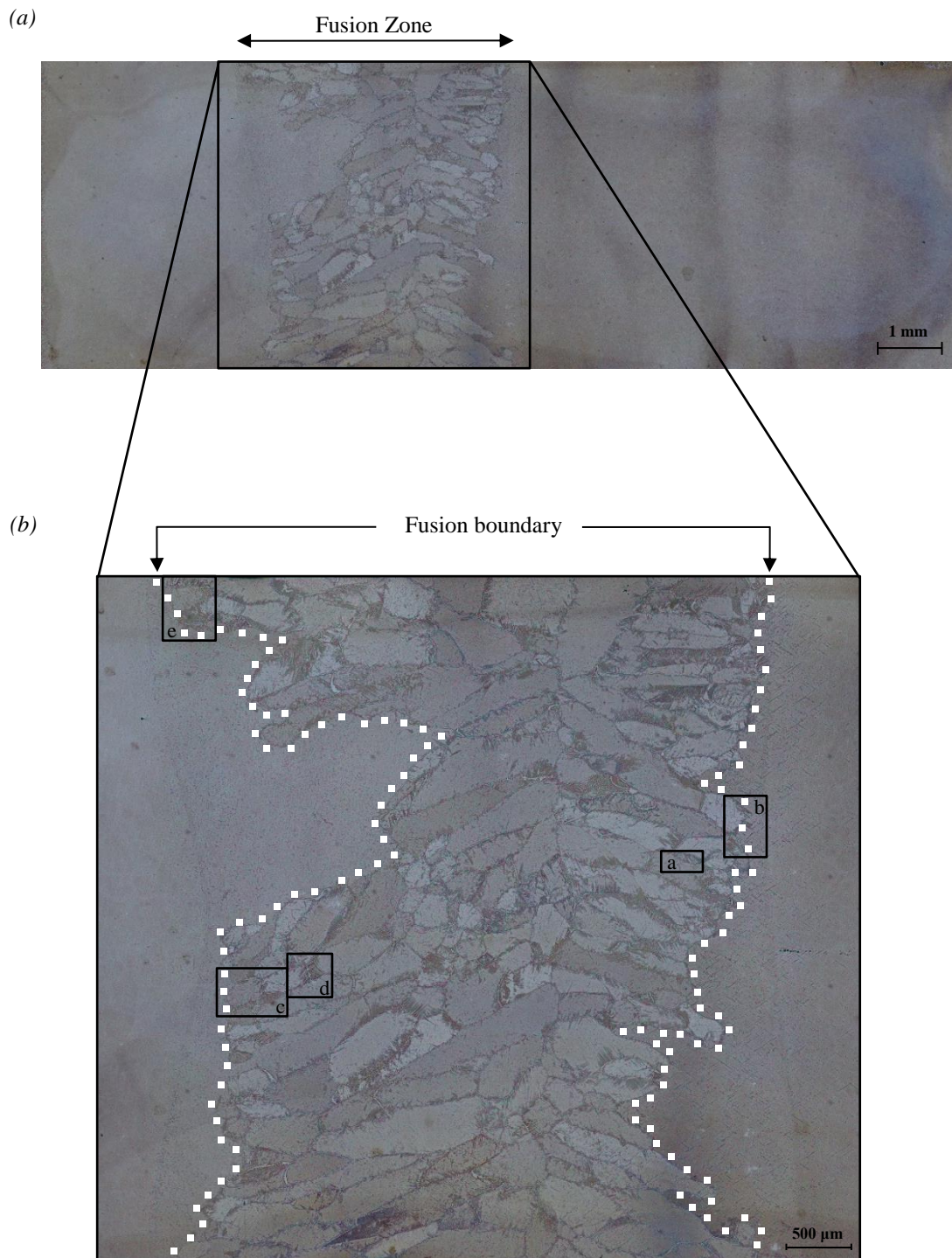
Figure 15 - (a) Macrograph of the welded Cu-Al-Mn similar joint. (b) Detailed macrograph of the fusion zone, with letters from "a" to "e" identifying a specific region.

The different colours observed within the fusion zone (Figure 15 (b)) are related to differences in grain orientation [20].

Figure 16 (b) and (c) shows the inverse pole figure orientation map obtained by electron back-scattered diffraction. The colours of each grain in the mapped microstructure indicate the crystallographic orientation displayed with the same colour as those in the reference of the stereographic triangle indicated in Figure 16 (a). EBSD observations allowed the confirmation of

the previous results (based only on colorimetric changes observed in optical microscopy). That is, the welded zone and the initial base material crystal have different grain orientations, where it can be observed that the grains present different colours and, consequently, different orientations. The columnar grains do not seem to have a preferential orientation, thus the welding process contributes to the development of near-random crystallographic texture within the fusion zone. Since the superelastic strain of single crystal SMAs strongly depends on the loading direction, texture control is important for enhancing their superelastic properties [16]. Previous studies have shown that the development of texture improves damping capacity, since textured specimens present damping properties two times higher than that of the random textured Cu-Al-Mn specimens [18].

(a)

(b)
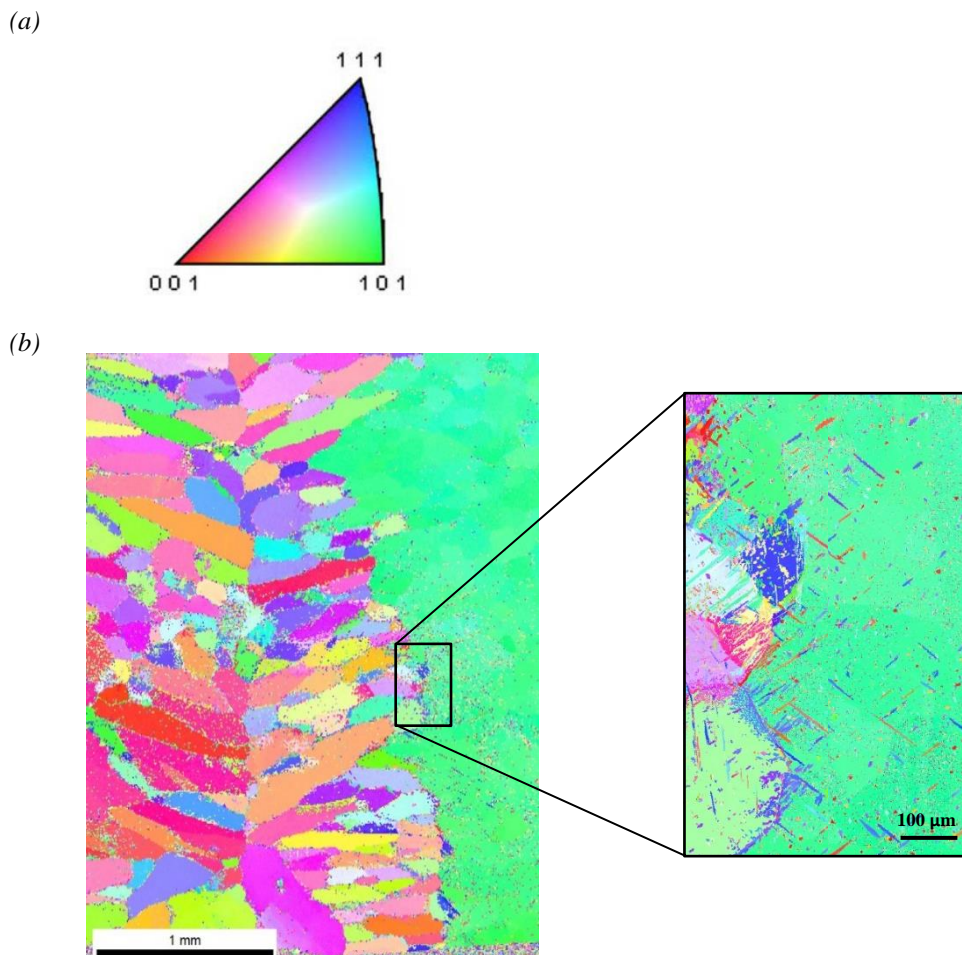
Figure 16 - (a) Unit stereographic triangle [20]. (b) EBSD Inverse Pole Figure orientation map. (c) Region "a" in detail.

Precipitation phenomena was observed in the fusion zone and heat affected zone (Figure 17 (b)). A large quantity of precipitates nucleated at the grain boundaries of the prior β-phase, or parent phase, showing needle shaped-like structures in the grain boundaries and within each grain (Figure 17). In some regions, this acicular morphology presents various sizes and shapes, while

in other regions is much longer and more ordered, for example in Figure 17 (d), presenting a Widmanstätten-like structure inside the grains. Widmanstätten structures have previously been observed in Cu-based shape memory alloys [43–47]. Widmanstätten needles form in the β-phase of metal alloys that have been cooled across the β/(α+β) phase boundary. The presence of this transformation is based on the width of the β-phase region reducing as the temperature reaches room temperature, due to the low cooling rates induced by high arc energy processes, such as GTAW [45].
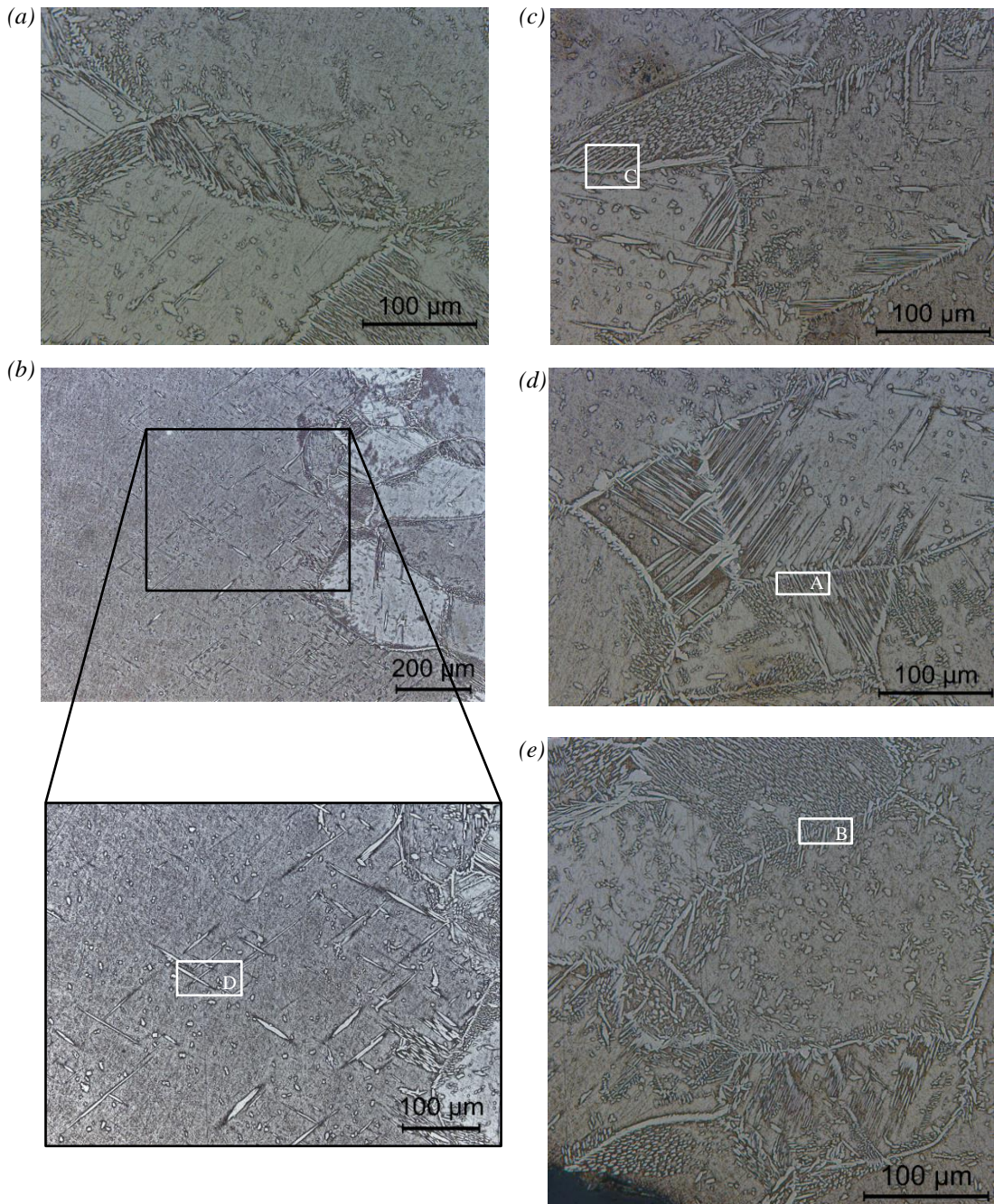
Figure 17 - Optical micrographs of the fusion zone in seven distinct regions, identified in Figure 15 (b). The letters from A to D inside de images, identify the SEM/EDS regions analysed within the FZ.

These results were confirmed by EBSD analysis, as shown in Figure 18, where the green regions indicate the presence of α-phase and the red regions indicate the presence of β-phase showing a α (face-centered cubic, fcc) + β (body-centered cubic, bcc) two-phase microstructure.

For the Cu-Al-Mn alloy, the presence of α-phase is disadvantageous, since this phase does not only prevent martensitic transformation and shape memory effect, but also embrittles the structure [48].
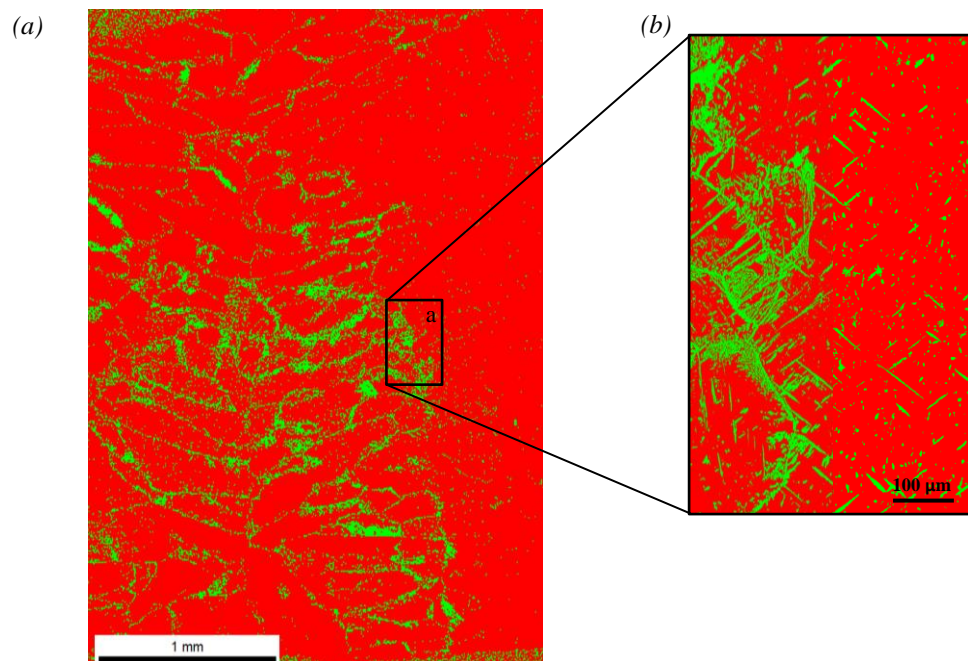
Figure 18 - a) EBSD Phase ID. b) Region "a" in detail.

4.3 Microstructural Characterization by Scanning Electron Microscopy/Energy Dispersive Spectroscopy

The compositional variation of all discernible phases after the welding process was determined by SEM-EDS analysis. A total of 18 spots within the fusion zone were analysed, as shown in Figure 19. The aim of this analysis was to determine if the formation of the α-phase was accompanied by a chemical composition change resulting from welding.

(A)

(B)

(C)

(D)
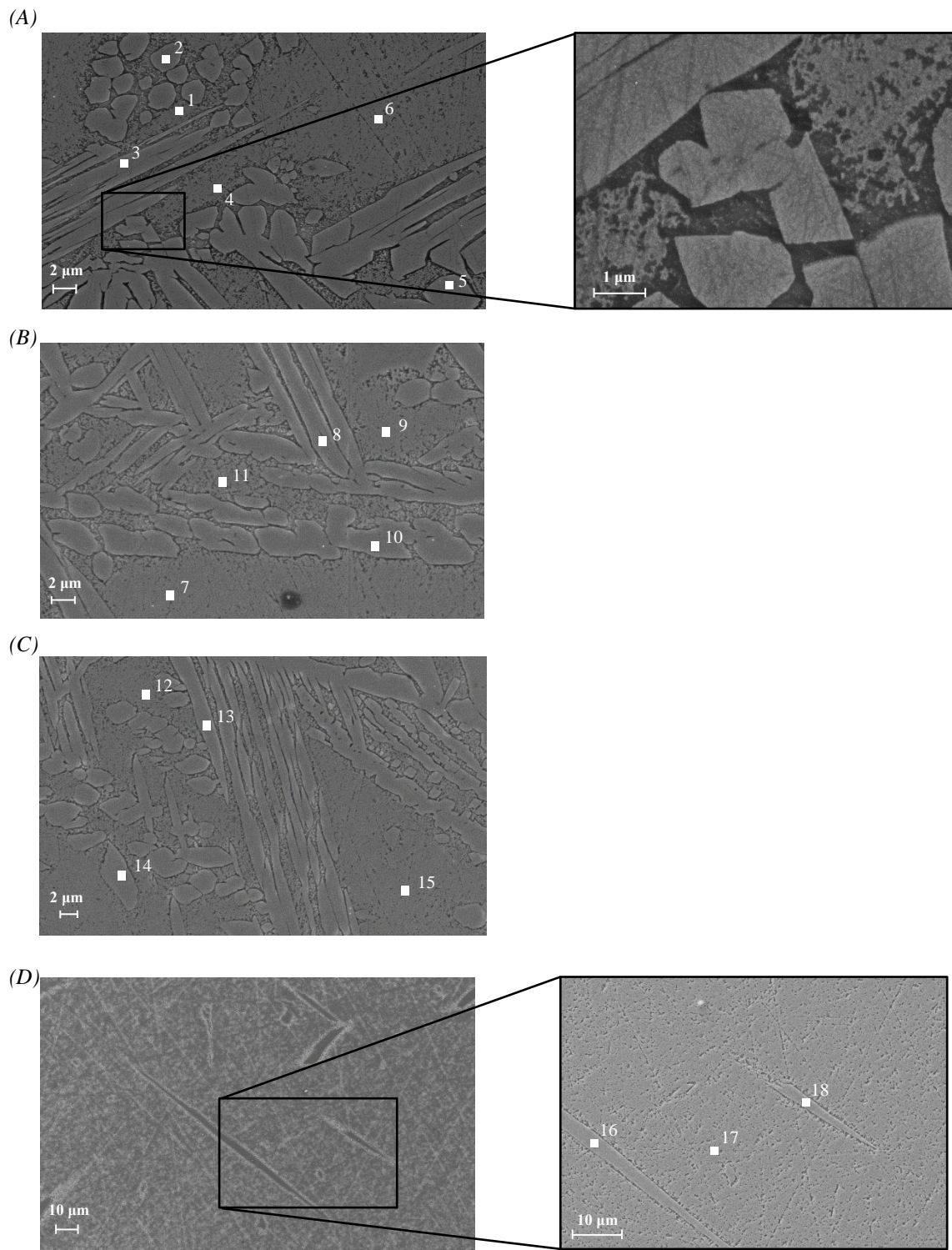
Figure 19 – SEM/EDS analysis of (A), (B), (C) and (D) regions.

Although α and β-phase are close in composition, compositional changes between the two regions were clearly observed. In comparison to the base material, the remaining β matrix, has a higher Al and Mn content, due to the precipitation of the α-phase, which is richer in Cu [47]. It is possible to observe this trend along the fusion zone from the graph depicted in Figure 20. The average chemical composition results of the two phases are presented in Table 5.

Table 5 - Average EDS measurements in the fusion zone.

Region	Cu [%]	Al [%]	Mn [%]
α-phase	71.46 ± 0.78	17.68 ± 0.75	10.86 ± 0.33
β-phase	67.87 ± 0.67	20.60 ± 0.57	11.53 ± 0.16
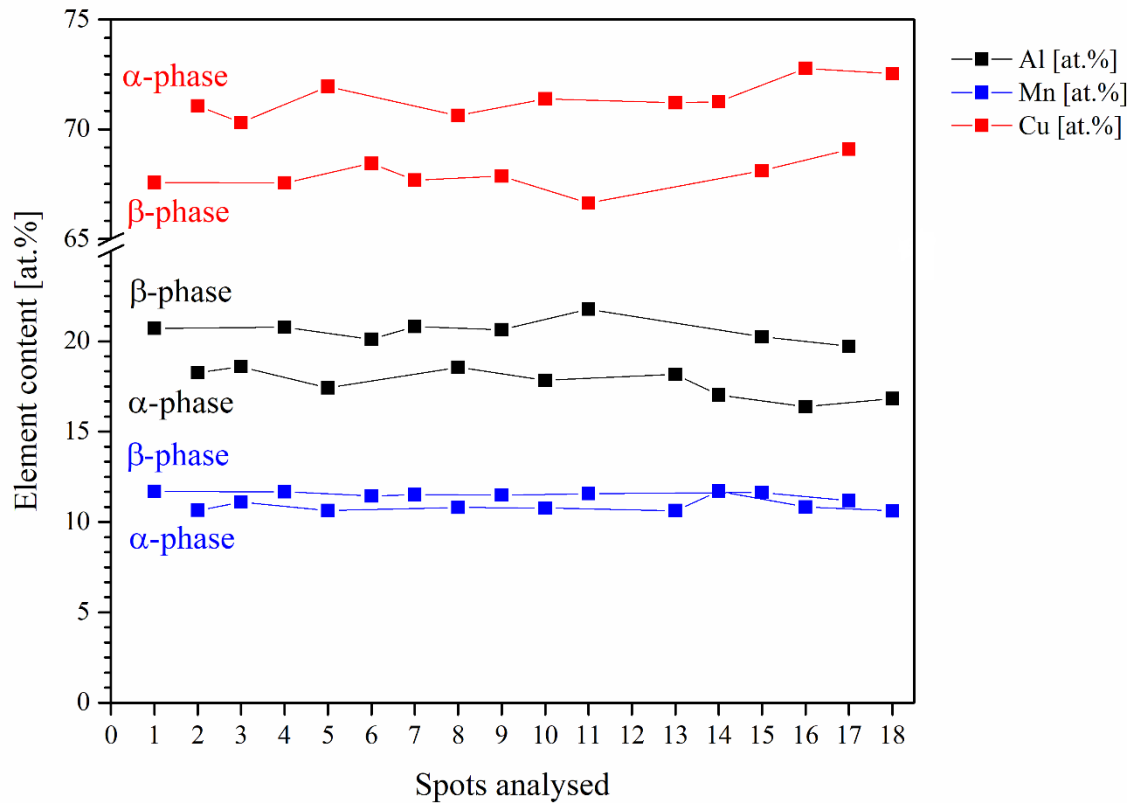
Figure 20 - Compositional profile across the fusion zone in the α and β-phase regions.

4.4 Microstructural Characterization by X-Ray Diffraction

X-ray diffraction analysis was used to determine the different phases formed in the welded specimen. The XRD pattern of the welded Cu-Al-Mn alloy is illustrated in Figure 21. By comparing results obtained with those published in the literature [42], the peaks in the patterns were identified. The main peak observed is the (200)β diffraction peak, along with less intense β-peaks and also α-phase peaks.

The X-ray diffraction results confirm the EBSD results: the weld metal exhibits a biphasic structure composed by β and α-phases.
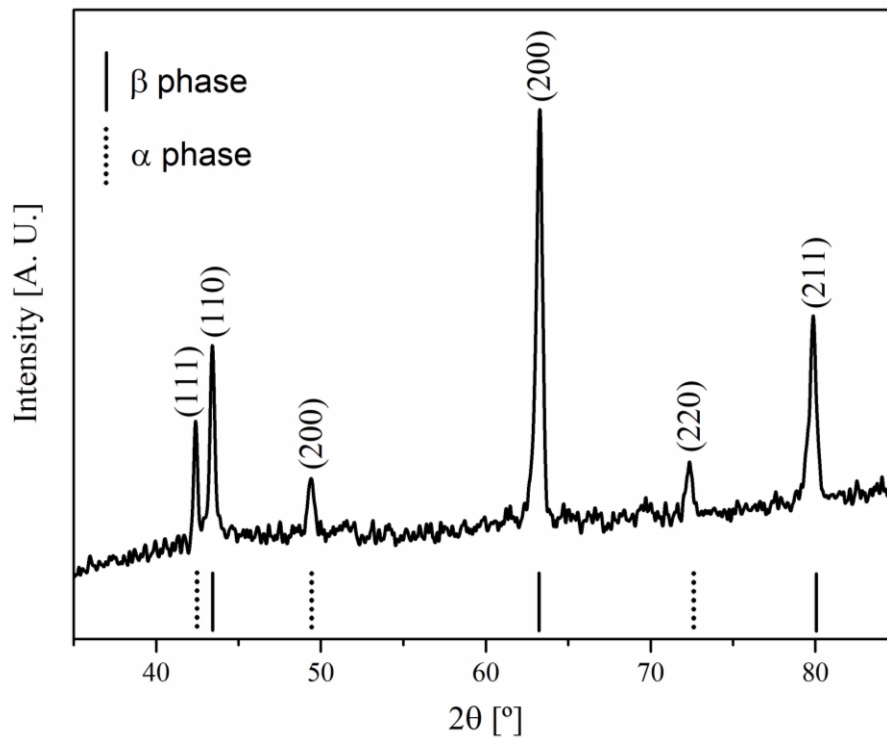
Figure 21 - X-ray diffraction pattern of the weld metal from the Cu-Al-Mn joint.

4.5 Microstructural Characterization using micro-Hardness Measurements

Hardness measurements were performed on seventeen lines throughout the base material and the fusion zone as schematically represented in Figure 22 (a) (only three hardness measurement lines are represented). A representative trend of the average hardness values of the regions analysed is shown in the graph, depicted in Figure 22 (b). A large scatter of hardness values was observed where significant hardness changes were found between the FZ and the HAZ. The inability to detect hardness variations between the base material and heat affected zone may be due to the effect of annealing heat treatments performed on the base material prior to welding. Observations from previous works, regarding laser welding of Cu-Al-based alloys, have shown the same inability [14,19,38]. Solely near the fusion zone boundary, a considerable variation of values is detected. The symmetric trend of the hardness measurements both on the right and on the left of the welded zone confirms the repeatability of the results. The base material average hardness was 223.9 ± 5.9 HV, while the fusion zone was 207.1 ± 10.9 HV. These values are within the hardness range expected for this alloy [49].

(a)
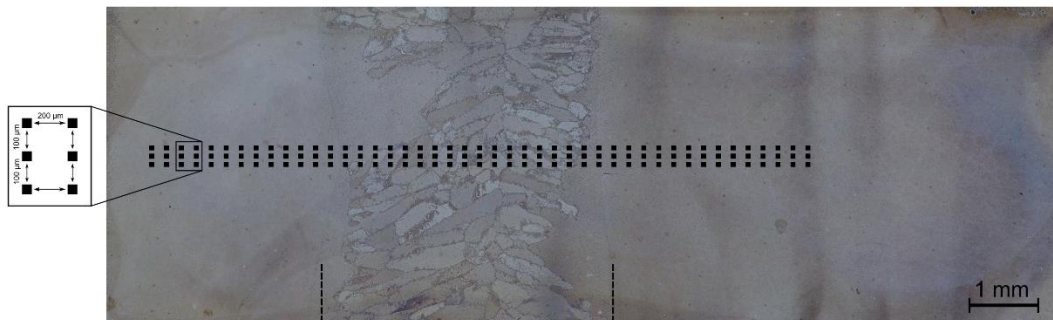
(b)
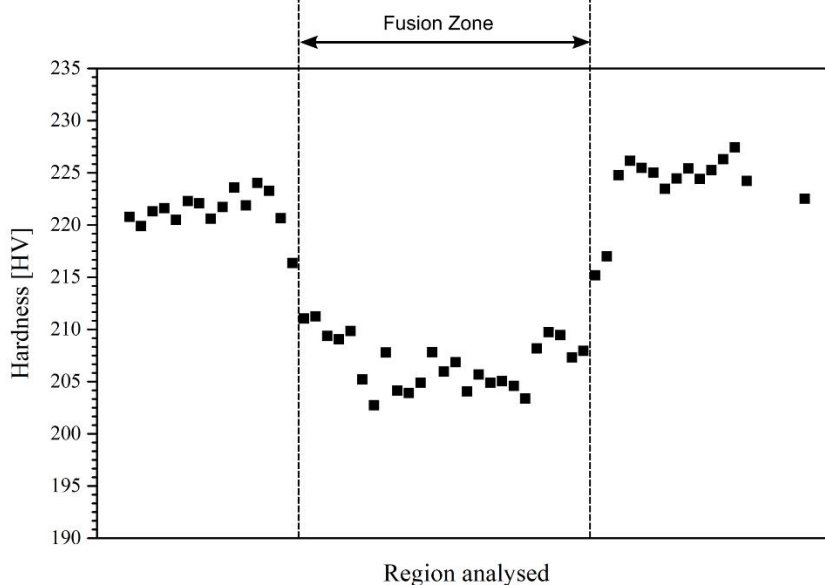
Figure 22 – (a) Optical macrograph of the welded specimen schematically showing the hardness measurements. (b) Corresponding average hardness values for the region analysed.

Figure 23 presents the microhardness map of the similar Cu-Al-Mn joint. A good agreement with the macrograph presented in Figure 22 (a) is evident, showing that in the fusion zone the hardness values are slightly lower than in the heat affected zone.
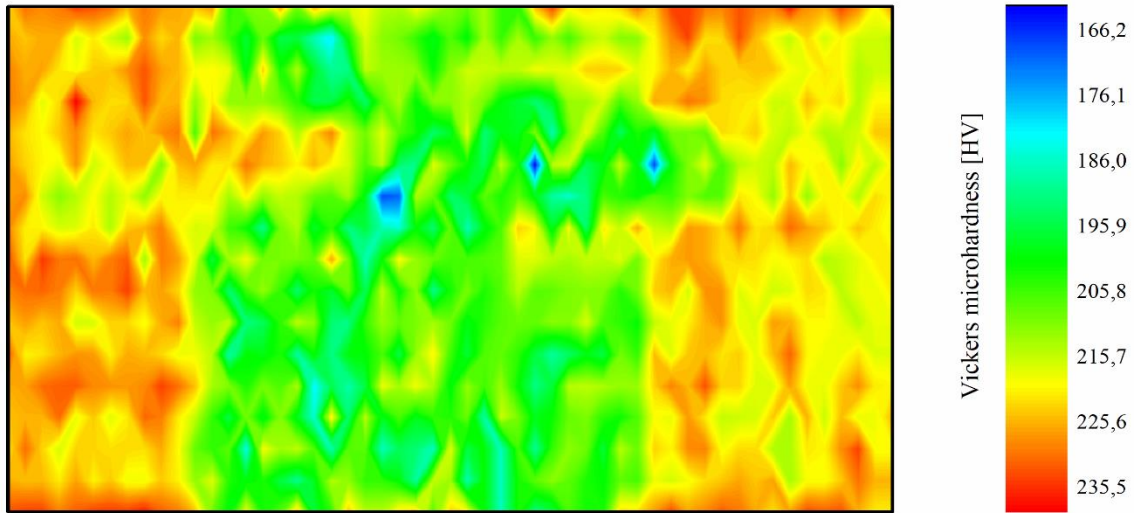
Figure 23 - Microhardness map of the Cu-Al-Mn similar joint.

4.6 Characterization of the Mechanical Properties

4.6.1 Tensile Tests

Uniaxial tensile tests were performed on both the base material and three welded specimens, (identified as weld 1, weld 2 and weld 3) to evaluate their mechanical properties. Figure 24 depicts the stress-strain curves obtained by tensile testing at room temperature. The ultimate tensile strength and elongation to fracture results are presented in Table 6.

It can be observed that the tensile curves of the welds are identical to that of the base material, with the average stress for inducing the martensitic transformation being similar for both base material and welded specimens: approximately 250 MPa. This maybe a reflexion of the reduced welded area in comparison to the total gauge length. The ultimate tensile strength of the base material (424.3 MPa) is lower than that of the welds 1 (445 MPa) and 3 (843.6 MPa), and slightly higher than weld 2 (360.2 MPa). The most striking observation is the significantly higher tensile strength presented by weld 3 when compared to the other tested specimens, which may be due to the dependence of crystal orientations and loading direction. In fact, within the gauge length of the tensile specimens the number of grains which are strained may vary. Since these alloys have very large grain size, any minor variation of the number of available grains within the gauge length can significantly alter their mechanical properties.

When the samples were subjected to tensile stress, the parent phase deformed elastically at first and then, with the stress increasing, the slope coefficient decreased, which indicated stress-induced martensite transformation from the parent-phase austenite. Subsequently, the slope coefficient increased, which indicated the elastic deformation and reorientation in stress-induced martensite and finally the slope coefficient decreases until the sample fractures [50]. Elongation to fracture values are higher in all the welded specimens, when compared to those of the base material, with fracture occurring at strain levels in the range of 31 to 38%. This can be related to the fusion zone microstructure as it will be discussed.
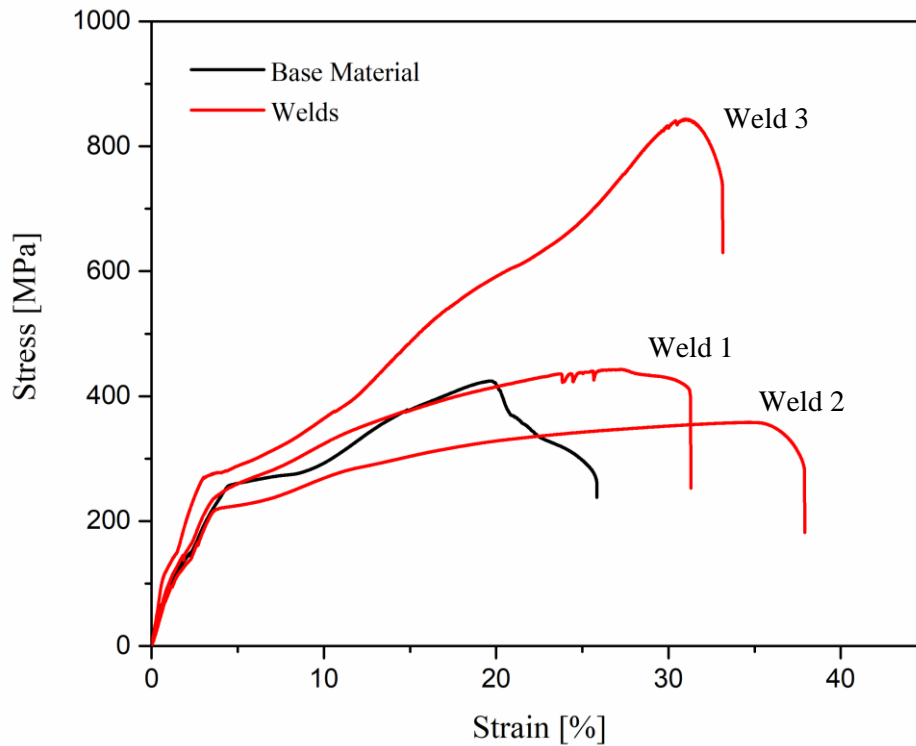
Figure 24 - Tensile behaviour of the Cu-Al-Mn base material and welded specimens.

Table 6 - Strength and ductility parameters from tensile test results.

Sample	UTS [MPa]	Elongation to fracture [%]
Base Material	424,3	25,8
Weld 1	445	31,3
Weld 2	360,2	37,9
Weld 3	843,6	33,1

Typically, when welding shape memory alloys, for instance NiTi, which is the most studied SMA, a decrease of the mechanical properties is noticeable due to grain growth [51–54]. That is not the case for Cu-Al-Mn shape memory alloys that do not appear to exhibit significant changes on the overall tensile properties of the welded joints, when compared to those of the base material [14,38], this is due to high temperature heat treatments used to induce the generally large grain size in the material. Thus, the temperature reached in the heat affected zone will have an almost negligible effect on the microstructure. As a result, no significant differences in the tensile behaviour of the welded material occur.

On the base material sample, significant necking was observed in the central region of the specimen where fracture occurred, as depicted in Figure 26. Remarkably, fracture of the welded specimens during tensile testing also occurred in the base material, distant from the fusion zone

(Figure 27). This is related with the fact that the relatively finer grain microstructure in the fusion zone can delay crack propagation, with the grains that present smaller sizes accommodating the load, leading this region to become less susceptible to intergranular cracking. On the other hand, in the single crystal base material, any crack that forms will propagate without any sort of blockage, such as grain boundaries. This explains the higher deformation until fracture of the welds [14,38].

Figure 25 illustrates different stages of the uniaxial tensile tests for the weld 2 specimen, until rupture, where significant necking can be observed. The different colours within the gauge length of the specimen give an indication of the number of grains that were being stressed in the base material (4 grains).
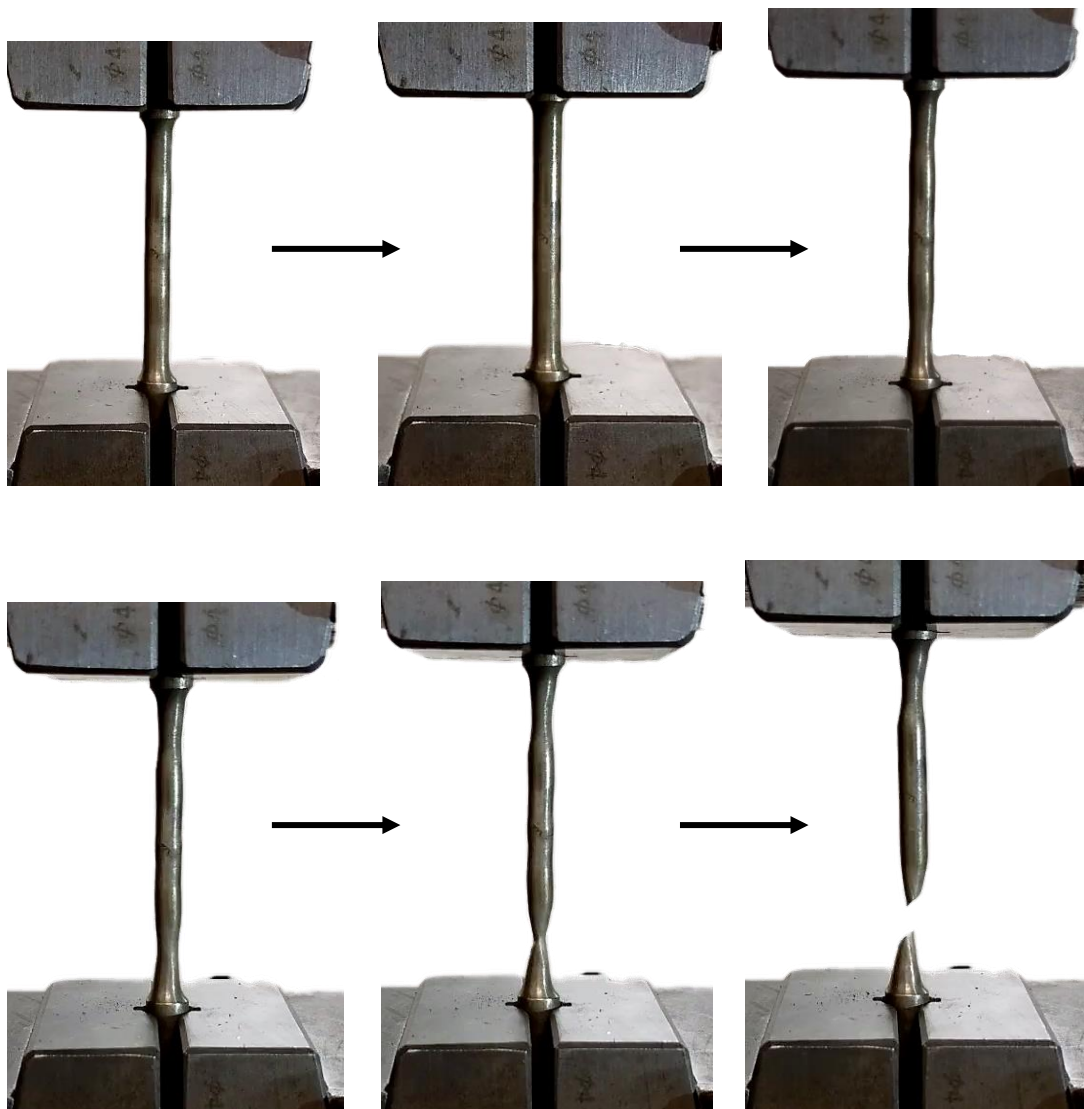
Figure 25 - Different stages of the uniaxial tensile test for weld 2 specimen.

After the uniaxial tensile tests, SEM analysis of the fracture surfaces of the base material and weld specimens was performed. These observations allow the understanding of the fracture morphology. Figures 26 (b) and 27 (b) show the fracture surface of the analysed samples, revealing a ductile-like fracture, as evidenced by the significant presence of dimples. No influence of the welding process was observed on the fracture surface, since fracture occurred in the non-affected base material.
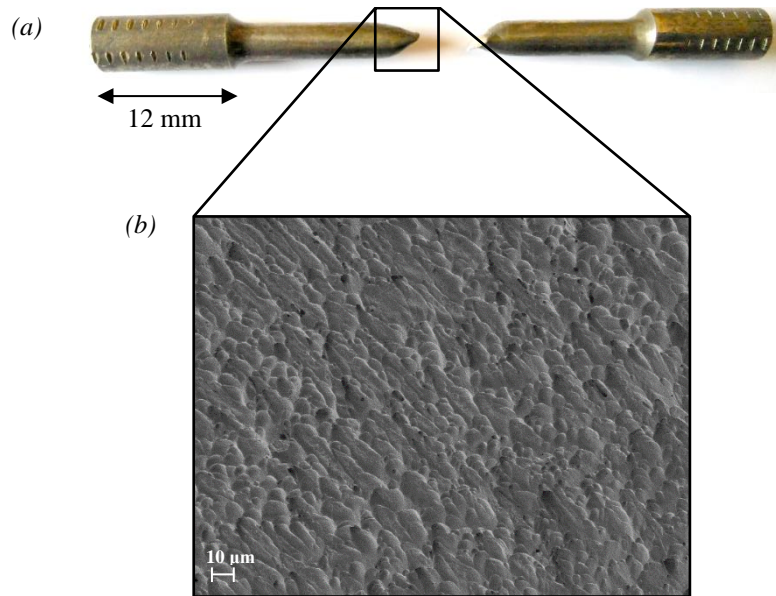
Figure 26 - (a) Base material after uniaxial tensile test. (b) Fracture surface of the base material.
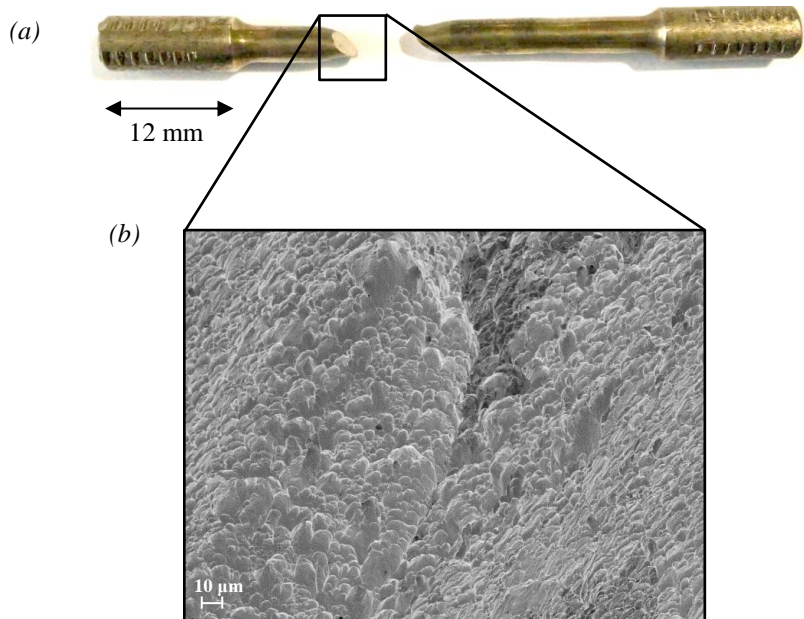
Figure 27 - (a) Welded specimen after uniaxial tensile test. (b) Fracture surface of the welded specimen.

4.6.2 Cycling Tests

High damping materials are attracting attention for engineering applications because of the increasing need for vibration and noise control reduction in various fields. For such applications, it is required that the selected materials are capable of absorbing substantial amounts of energy, when subjected to load variations, such as seismic devices [12,23]. Therefore, the understanding of the load/unload cycling behaviour of the welded joints and its repeatability is fundamental to evaluate the viability of their use in such applications. For shape memory alloys, energy dissipation is usually performed in the superelastic regime. Ideally, any imposed external deformation can be fully restored, upon unloading.

Due to their lower production costs when compared to NiTi alloys, Cu-based shape memory alloys are being considered as substitutes for NiTi in energy-absorption devices [12,23–25].

In the present study a welded joint and the base material, for reference, were subjected to a cycling routine to evaluate their superelastic properties, where the rod was loaded with a maximum imposed strain of 8%, then unloaded to a zero-stress condition. This procedure was repeated until 100 mechanical load/unload cycles were performed. Figure 28 (a) and (b) shows the cyclic stress-strain curves for both base material and welded specimen, respectively. The overlap of the two curves is depicted in Figure 28 (c). The start of the martensitic transformation occurs approximately at the same values of the previous tensile tests. Furthermore, the superelastic curve typical of SMAs is clear after the welding process.

(a)

(b)

(c)
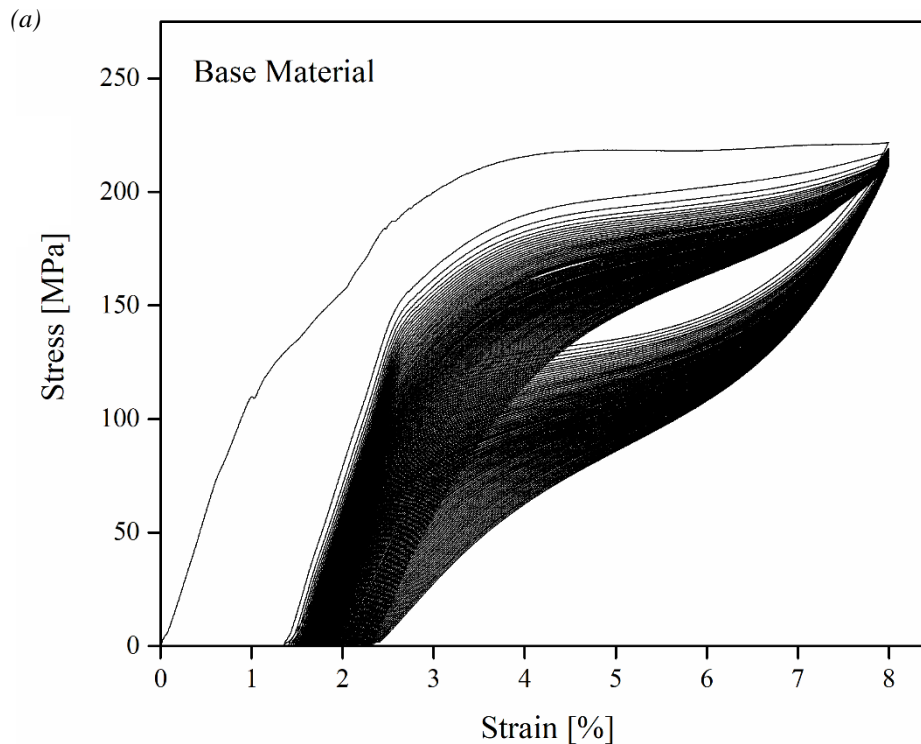
Figure 28 - Cycling behaviour of: (a) the base material; (b) the welded specimen. (c) Overlap of base material and welded specimen cycling behaviours.

From the load/unload behaviour of the joints it is possible to determine the evolution of the accumulated irrecoverable strain and absorbed energy per cycle of the Cu-Al-Mn weld, as depicted in Figure 29.
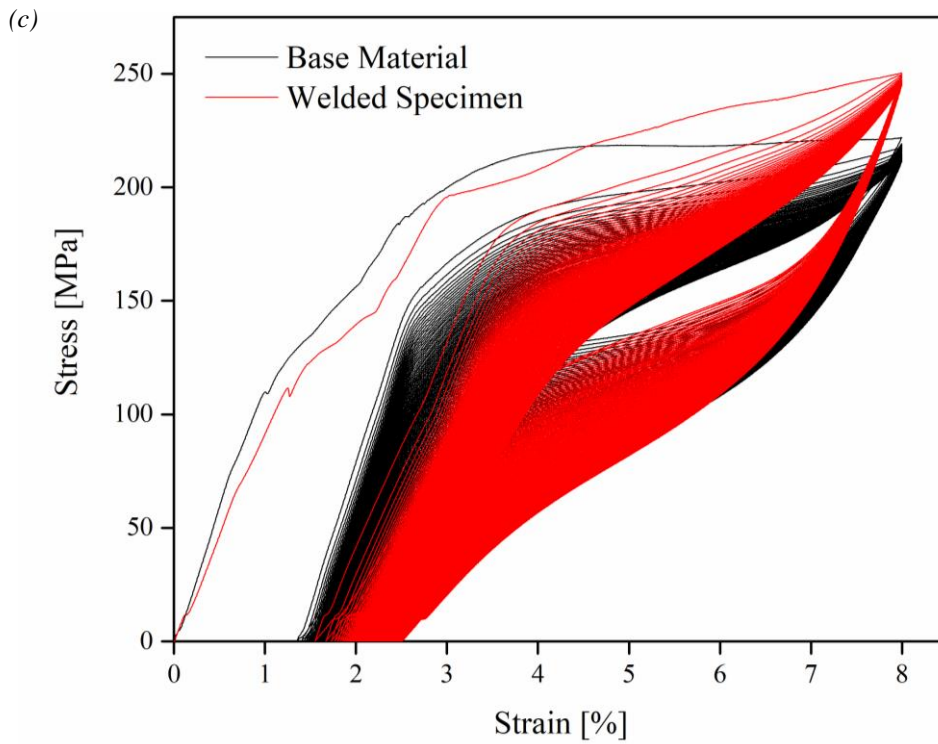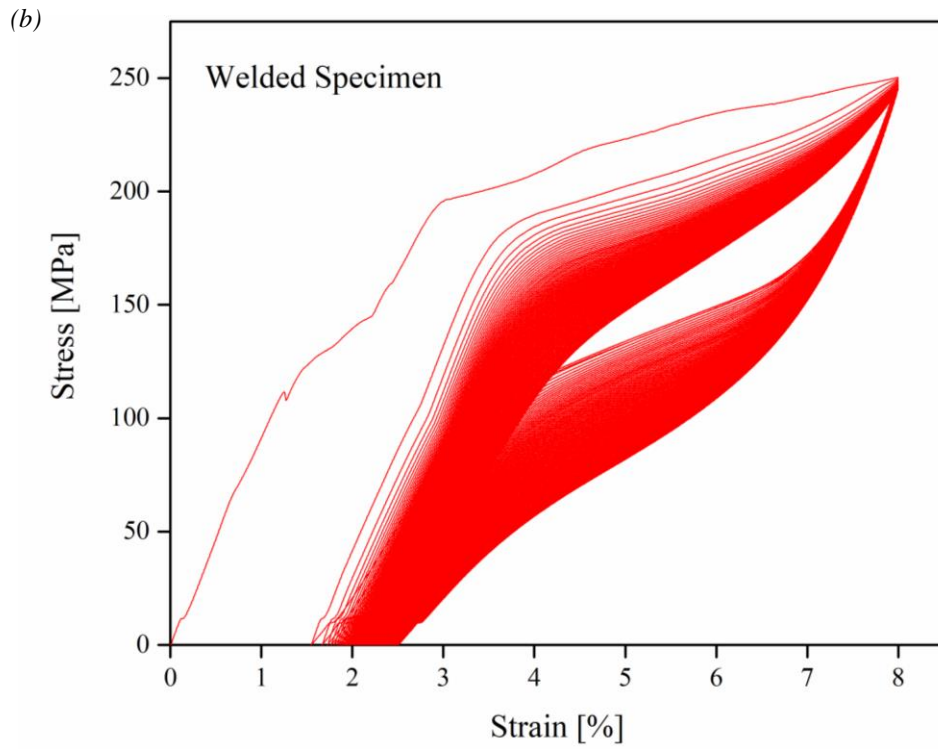
There are no significant differences between the cycling behaviour of the welded and base material specimens. The irrecoverable strain after the first cycle for the base material was around 1.3%. For the welded specimens a slightly higher value for the irrecoverable strain after the first cycle was observed, around 1.5%. The presence of multiple factors can affect the superelastic response of the Cu-Al-Mn alloy. These can include grain size and grain orientation. The slightly larger irrecoverable strain in the welded specimen can be attributed to: the finer grained fusion zone, which has smaller d/D ratio than the base material, which reduces the superelastic recovery upon unloading [20]. In Cu-based shape memory alloys, the recoverable strain depends on the grain size (d) relative to the size of the specimen, for sheet thickness (t) or wire diameter (D), and increases with increasing the relative grain size, defined by the relation d/t or d/D. The superelastic strain increases with increasing d/D, owing to the fact that the free surface grain boundary area also increases, which is equal to the relaxation of the grain constraint [20]. Another reason that can justify the higher irrecoverable strain is related to the presence of α-phase which does not contribute to the superelastic behaviour and to the grain orientation in the fusion zone, which is clearly distinct from the optimized texture of the base material [38].

From Figure 29, it can also be observed that the first cycle has the higher absorbed energy, which is caused by the higher irrecoverable strain. After this, the hysteric loop which gives a measure of the absorbed energy per cycle, started to stabilize both in the base material and in the welded sample. The use of the superelastic effect in applications, typically requires that the cycling behaviour along a given load/unload path is stabilized after a given number of cycles.

Of special interest is the evolution of the accumulated irrecoverable strain with the number of cycles. For the welded specimen, the irrecoverable strain had a steady increase after 20 load/unload cycles. In opposition, for the base material after 60 load/unload cycles a sharp change in the evolution of the accumulated irrecoverable strain was observed. In fact, the functional fatigue of the base material tends to be more important than in the welded joint, since the intersection between the two curves would occur at around 110 cycles, after which the irrecoverable strain of the base material would surpass that of the welded joint. In this case, the presence of a refined grain structure in the fusion zone can contribute to this effect: with more grain boundaries in the material, the movement of dislocations during the stress-induced transformation is harder, thus resulting in a higher resistance to functional fatigue than in the base material.
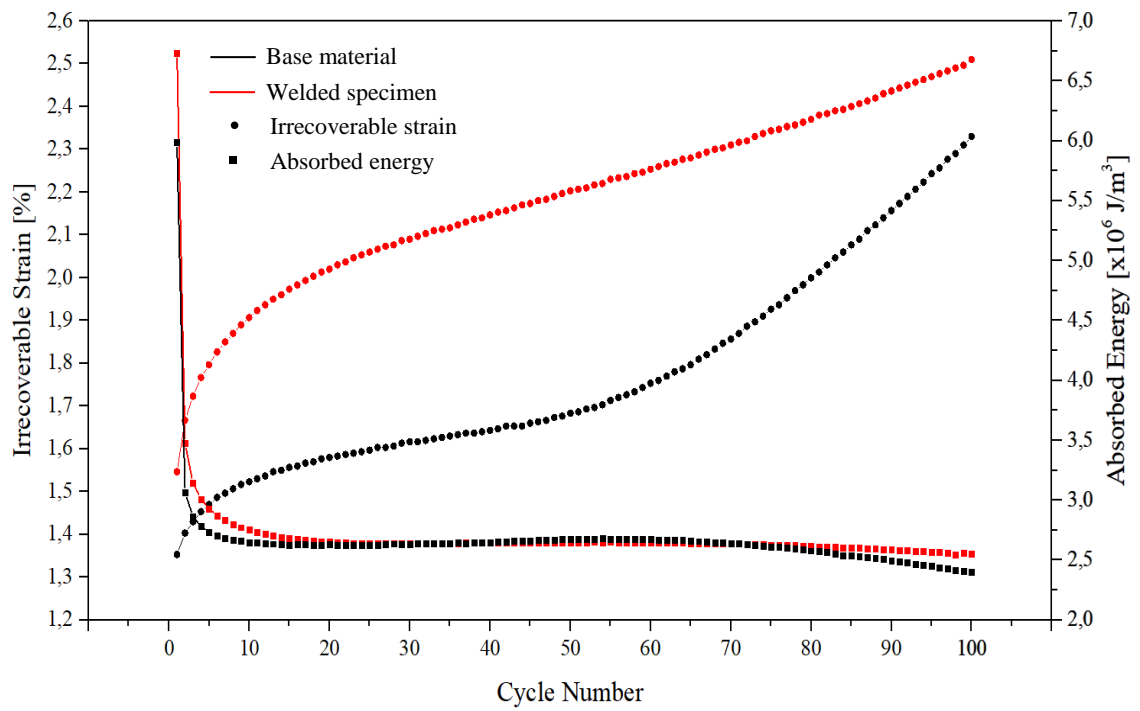
Figure 29 - Evolution of the accumulated irrecoverable strain and absorbed energy with the number of cycles for the base material and the welded specimen.

5

Conclusions and Future work

In this study, the first reported Cu-Al-Mn similar joints were produced by gas tungsten arc welding. The present work contributed to a deeper understanding of the effects of arc-based welding on the microstructure and mechanical properties of Cu-Al-Mn shape memory alloys. Based on the results obtained the following can be concluded:

- The superelastic Cu-Al-Mn presented good weldability and a precise control of the welding parameters is extremely important to allow the production of quality welds.

- Within the fusion zone the grains did not seem to have preferential orientation, thus the welding process contributed to the development of near-random crystallographic texture. EBSD observations allowed the confirmation that the welded zone and the initial base material crystal have different grain orientations

- The GTAW process is responsible for inducing microstructural changes in the thermally affected regions. Precipitation phenomena of α-phase was observed in the fusion zone and heat affected zone. The slow cooling of the material after the arc was extinguished is responsible for the α-phase precipitation. In some regions, the precipitates presented various shapes and sizes, while in other regions they presented a Widmanstätten-like structure inside the grains, due to the low cooling rates induced by high arc energy processes, such as GTAW.

- A large scatter of hardness values was observed where significant hardness changes were found between the fusion zone and the heat affected zone.

- SEM/EDS analysis results showed that in comparison to the base material, the remaining β matrix had a higher Al and Mn content, due to the precipitation of the α-phase, richer in Cu.

- No significant changes of the overall tensile properties of the welded specimens were observed, when compared to the base material. It can be observed that the tensile curves of the welds are identical to that of the base material. Fracture of the base material and welded specimens during tensile testing occurred in the base material. Fracture surface analysis of the tested samples revealed a ductile-like fracture.

- There were no significant differences between the cycling behaviour of the welded and base material specimens. After the first cycle, the irrecoverable strain of both materials rapidly reduced to a stabilized value.

Although the main objectives of this work were achieved, opportunities for further investigation were identified, namely:

- Analysis of the effects of different welding parameters on the mechanical behaviour of the similar Cu-Al-Mn joints.

- Assessment of the fatigue strength of the welded specimens and its correlation with the welding parameters. Different cycling routines could also be studied.

- Development of an energy absorption system based on Cu-Al-Mn joints.

- Bead-on-plate welds were performed, to avoid the variability of joint fit-up. Therefore, these design parameters should be studied in the future.

- Evaluating the possibility of joining Cu-Al-Mn SMA to other materials, since it is fundamental for the development of new applications.

References

[1]   D.C. Lagoudas, Shape Memory Alloys, New York: Springer, 2008. doi:10.1007/978-0-387-47685-8.

[2]   K. Otsuka, C.M. Wayman, Shape Memory Materials, Cambrigde University Press, 1998.

[3]   L.C. Chang, T.A. Read, No Title, Trans AIME. (1951).

[4]   W.J. Buehler, J. V. Gilfrich, R.C. Wiley, Effect of low temperature phase changes on the mechanical properties of alloys near composition NiTi, J. Appl. Phys. 34 (1963) 1475–1477.

[5]   J.L. Liu, H.Y. Huang, J.X. Xie, Superelastic anisotropy characteristics of columnar-grained Cu-Al-Mn shape memory alloys and its potential applications, Mater. Des. 85 (2015) 211–220. doi:10.1016/j.matdes.2015.06.114.

[6]   K. Otsuka, X. Ren, Physical metallurgy of Ti-Ni-based shape memory alloys, Prog. Mater. Sci. 50 (2005) 511–678. doi:10.1016/j.pmatsci.2004.10.001.

[7]   Y. Sutou, T. Omori, R. Kainuma, K. Ishida, Ductile Cu–Al–Mn based shape memory alloys: general properties and applications, Mater. Sci. Technol. 24 (2008) 896–901. doi:10.1179/174328408X302567.

[8]   J.P. Oliveira, R.M. Miranda, F.M. Braz Fernandes, Welding and Joining of NiTi Shape Memory Alloys: A Review, 88 (2017) 412–466. doi:10.1016/j.pmatsci.2017.04.008.

[9]   J. Seo, Y. Kim, J. Hu, Pilot Study for Investigating the Cyclic Behavior of Slit Damper Systems with Recentering Shape Memory Alloy (SMA) Bending Bars Used for Seismic Restrainers, Appl. Sci. 5 (2015) 187–208. doi:10.3390/app5030187.

[10]   J.P. Oliveira, F. B. Fernandes, M. Miranda, Laser Welding of Shape Memory Alloys, Universidade Nova de Lisboa, 2016.

[11]   M. Dolce, D. Cardone, Mechanical behaviour of shape memory alloys for seismic applications 2. Austenite NiTi wires subjected to tension, Int. J. Mech. Sci. 43 (2001) 2657–2677. doi:10.1016/S0020-7403(01)00050-9.

[12]   Y. Araki, N. Maekawa, K.C. Shrestha, M. Yamakawa, Y. Koetaka, T. Omori, Feasibility of tension braces using Cu-Al-Mn superelastic alloy bars, Struct. Control Heal. Monit. 21. 19 (2014) 88–106. doi:10.1002/stc.

[13]   R. Kainuma, N. Satoh, J.X. Liu, I. Ohnuma, K. Ishida, Phase equilibria and Heusler phase stability in Cu-rich portion of the Cu-Al-Mn system, J. Alloy. Compd. 266. (1998) 191–200.

[14]   J.P. Oliveira, B. Panton, Z. Zeng, T. Omori, Y. Zhou, R.M. Miranda, F.M. Braz Fernandes, Laser welded superelastic Cu–Al–Mn shape memory alloy wires, Mater. Des. 90 (2016) 122–128. doi:10.1016/j.matdes.2015.10.125.

[15]   A. Planes, E. Obrado, Order-disorder transitions of Cu-Al-Mn shape-memory alloys, 58

(1998).

[16]   Y. Sutou, T. Omori, J.J. Wang, R. Kainuma, K. Ishida, Characteristics of Cu-Al-Mn-based shape memory alloys and their applications, Mater. Sci. Eng. A. 378 (2004) 278–282. doi:10.1016/j.msea.2003.12.048.

[17]   R. Kainuma, S. Takahashi, K. Ishida, No Title, J. Phys. IV 5. (1995) 961– 966.

[18]   Y. Sutou, T. Omori, N. Koeda, R. Kainuma, K. Ishida, Effects of grain size and texture on damping properties of Cu-Al-Mn-based shape memory alloys, Mater. Sci. Eng. A. 438–440 (2006) 743–746. doi:10.1016/j.msea.2006.02.085.

[19]   J.P. Oliveira, Z. Zeng, T. Omori, N. Zhou, R.M. Miranda, F.M.B. Fernandes, Improvement of damping properties in laser processed superelastic Cu-Al-Mn shape memory alloys, Mater. Des. 98 (2016) 280–284. doi:10.1016/j.matdes.2016.03.032.

[20]   Y. Sutou, T. Omori, K. Yamauchi, N. Ono, R. Kainuma, K. Ishida, Effect of grain size and texture on pseudoelasticity in Cu-Al-Mn-based shape memory wire, Acta Mater. 53 (2005) 4121–4133. doi:10.1016/j.actamat.2005.05.013.

[21]   J. Van Humbeeck, Non-medical applications of shape memory alloys, Mater. Sci. Eng. A. 273–275 (1999) 134–148. doi:10.1016/S0921-5093(99)00293-2.

[22]   S. Pareek, Y. Suzuki, Y. Araki, M.A. Youssef, M. Meshaly, Plastic hinge relocation in reinforced concrete beams using Cu-Al-Mn SMA bars, Eng. Struct. 175 (2018) 765–775. doi:10.1016/j.engstruct.2018.08.072.

[23]   Y. Araki, N. Maekawa, T. Omori, Y. Sutou, R. Kainuma, K. Ishida, Rate-dependent response of superelastic Cu-Al-Mn alloy rods to tensile cyclic loads, Smart Mater. Struct. 21 (2012). doi:10.1088/0964-1726/21/3/032002.

[24]   Y. Araki, T. Endo, T. Omori, Y. Sutou, Y. Koetaka, R. Kainuma, K. Ishida, Potential of superelastic Cu–Al–Mn alloy bars for seismic applications, (2010) 107–115. doi:10.1002/eqe.

[25]   B. Gencturk, Y. Araki, T. Kusama, T. Omori, R. Kainuma, F. Medina, Loading rate and temperature dependency of superelastic Cu-Al-Mn alloys, Constr. Build. Mater. 53 (2014) 555–560. doi:10.1016/j.conbuildmat.2013.12.002.

[26]   K. Weinert, V. Petzoldt, Machining of NiTi based shape memory alloys, Mater. Sci. Eng. A. 378 (2004) 180–184. doi:10.1016/j.msea.2003.10.344.

[27]   L. Quintino, R.M. Miranda, Welding shape memory alloys with NdYAG lasers, Soldag. Inspeção. 17 (2012) 210–217. doi:10.1590/S0104-92242012000300005.

[28]   H.M. Hobart, U.S. Patent 1,746,081, 1930.

[29]   P.K. Devers, U.S. Patent 1,746,191, 1930.

[30]   C.L. Jenney, A. O'Brien, Welding handbook, 1991. doi:10.1017/CBO9781107415324.004.

[31]   R. Meredith, 2,274,631, 1942.

[32] E.M.D.L. and R.M. Miranda, Metalurgia da Soldadura, Lisboa, 1993.

[33] J.N. Pires, A. Loureiro, T. Godinho, P. Ferreira, B. Fernando, J. Morgado, Welding robots, 2003. doi:10.1109/MRA.2003.1213616.

[34] S. Edition, Metallurgy Second Edition Welding Metallurgy, 2003. doi:10.1016/j.theochem.2007.07.017.

[35] G. Fox, R. Hahnlen, M.J. Dapino, Fusion welding of nickel-titanium and 304 stainless steel tubes: Part II: tungsten inert gas welding, J. Intell. Mater. Syst. Struct. 24 (2013) 962–972. doi:10.1177/1045389X12461076.

[36] J.P. Oliveira, B. D., B.F.F., M. M. R., Tungsten inert gas (TIG) welding of Ni-rich NiTi plates: functional behavior, (2016).

[37] A. Ikai, K. Kimura, H. Tobushi, TIG welding and shape memory effect of TiNi shape memory alloy, J. Intell. Mater. Syst. Struct. 7 (1996) 646–655. doi:10.1177/1045389X9600700604.

[38] J.P. Oliveira, Z. Zeng, S. Berveiller, D. Bouscaud, F.M. Braz Fernandes, R.M. Miranda, N. Zhou, Laser welding of Cu-Al-Be shape memory alloys: Microstructure and mechanical properties, Mater. Des. 148 (2018) 145–152. doi:10.1016/j.matdes.2018.03.066.

[39] C.A. Biffi, R. Casati, B. Previtali, A. Tuissi, Microstructure and mechanical properties of laser welded beads realized for joining CuZn open cellular foams, Mater. Lett. 181 (2016) 132–135. doi:10.1016/j.matlet.2016.05.161.

[40] J.P. Oliveira, Z. Zeng, C. Andrei, F.M. Braz Fernandes, R.M. Miranda, A.J. Ramirez, T. Omori, N. Zhou, Dissimilar laser welding of superelastic NiTi and CuAlMn shape memory alloys, Mater. Des. 128 (2017) 166–175. doi:10.1016/j.matdes.2017.05.011.

[41] TELWIN - Welding Technologies. Available: http://www.telwin.com/en/prodotti/?id=852030&clmer=81&clpro=02&cltec=03&clali= 01&lingua=E&descProdotto=TECHNOLOGY TIG 182 AC/DC

[42] R. Kainuma, S. Takahashi, K. Ishida, Thermoelastic Martensite and Shape Memory Effect in Ductile Cu-AI-Mn Alloys, Metall. Mater. Trans. A. 27A (1996) 2187–2195. https://link.springer.com/content/pdf/10.1007%2FBF02651873.pdf.

[43] L.G. Bujoreanu, Shape Memory Alloys: Manufacture, Properties and Applications, Nova Science Publishers, Inc., New York.

[44] L.G. Bujoreanu, On the influence of austenitization on the morphology of α-phase in tempered Cu-Zn-Al shape memory alloys, Mater. Sci. Eng. A. 481–482 (2008) 395–403. doi:10.1016/j.msea.2006.12.223.

[45] V.K. Bhatia, C.S. Kealley, R. Wuhrer, K.S. Wallwork, M.B. Cortie, Ternary β and γ phases in the Al-Au-Cu system at 750 °C, J. Alloys Compd. 488 (2009) 100–107. doi:10.1016/j.jallcom.2009.08.129.

[46] A. Kostov, A. Milosavljevic, Z.S. Simsic, C. Craciunescu, Characterization of Copper-Based Shape Memory Alloy with Zinc and Aluminum, (2018) 36–43.

[47] J.M. Guilemany, J. Fernández, Relationships between structure and hardness developed during the high temperature ageing of a smart Cu-based alloy, J. Mater. Sci. 31 (1996) 4981–4984. doi:10.1007/BF00355890.

[48] M. Zare, M. Ketabchi, Effect of chromium element on transformation, mechanical and corrosion behavior of thermomechanically induced Cu–Al–Ni shape-memory alloys, J. Therm. Anal. Calorim. 127 (2017) 2113–2123. doi:10.1007/s10973-016-5839-2.

[49] Y. Sutou, N. Koeda, T. Omori, R. Kainuma, K. Ishida, Effects of aging on stress-induced martensitic transformation in ductile Cu-Al-Mn-based shape memory alloys, Acta Mater. 57 (2009) 5759–5770. doi:10.1016/j.actamat.2009.08.011.

[50] Y. Jiao, H. Zhang, T. Zhang, Effect of Al Content and Annealing Temperature on Cold Workability of CuAlMn Alloys, IOP Conf. Ser. Mater. Sci. Eng. 381 (2018) 012153. doi:10.1088/1757-899X/381/1/012153.

[51] C.W. Chan, H.C. Man, T.M. Yue, Effects of process parameters upon the shape memory and pseudo-elastic behaviors of laser-welded NiTi thin foil, Metall. Mater. Trans. A Phys. Metall. Mater. Sci. 42 (2011) 2264–2270. doi:10.1007/s11661-011-0623-1.

[52] Y.G. Song, W.S. Li, L. Li, Y.F. Zheng, The influence of laser welding parameters on the microstructure and mechanical property of the as-jointed NiTi alloy wires, Mater. Lett. 62 (2008) 2325–2328. doi:10.1016/j.matlet.2007.11.082.

[53] a Tuissi, S. Besseghini, T. Ranucci, F. Squatrito, M. Pozzi, Effect of Nd-YAG laser welding on the functional properties of the Ni–49.6at.%Ti, Mater. Sci. Eng. A. 273–275 (1999) 813–817. doi:10.1016/S0921-5093(99)00422-0.

[54] H. Gugel, A. Schuermann, W. Theisen, Laser welding of NiTi wires, Mater. Sci. Eng. A. 481–482 (2008) 668–671. doi:10.1016/j.msea.2006.11.179.

Appendix A – Technical drawings of the machined rods

Technical drawing labels:

R3

Ø4

Ø6

30

32

60

UNLESS OTHERWISE SPECIFIED:
DIMENSIONS ARE IN MILLIMETERS
SURFACE FINISH:
TOLERANCES:
 LINEAR:
 ANGULAR:

FINISH:

DEBURR AND
BREAK SHARP
EDGES

DO NOT SCALE DRAWING

REVISION

	NAME	SIGNATURE	DATE			TITLE:
DRAWN						
CHK'D						
APPV'D						
MFG						
Q.A			MATERIAL:		DWG NO.	

Provete Cu-Al-Mn

A4

WEIGHT:

SCALE:1:1

SHEET 1 OF 1